The Astrophysical Journal, 1002:54 (17pp), 2026 May 1 https://doi.org/10.3847/1538-4357/ae4c87

WFST Supernovae in the First Year. II. SN 2024aedt: Systematical Study of a Transitional Type Ia Supernova

Dezheng Meng[1,2], Ji-an Jiang[1,3], Xu Kong[1,2,4], Zelin Xu[1,2], Keiichi Maeda[5], Hanindyo Kuncarayakti[6,7], Lluís Galbany[8,9], Saurabh W. Jha[10], Željko Ivezić[11], Peter Yoachim[11], Weiyu Wu[1,2], Zhengyan Liu[1], Junhan Zhao[1,2], Andrew J. Connolly[11], Ziqing Jia[1], Lei Hu[12], Weiyu Ding[1,2], Lulu Fan[1,4], Feng Li[13], Ming Liang[14], Jinlong Tang[15], Zhen Wan[1], Hairen Wang[16], Jian Wang[13,4], Yongquan Xue[1], Hongfei Zhang[13], Wen Zhao[1], Xianzhong Zheng[17], and Qingfeng Zhu[1,4]

[1] Department of Astronomy, University of Science and Technology of China, Hefei 230026, People's Republic of China; jian.jiang@ustc.edu.cn, xkong@ustc.edu.cn
[2] School of Astronomy and Space Sciences, University of Science and Technology of China, Hefei 230026, People's Republic of China
[3] National Astronomical Observatory of Japan, 2-21-1 Osawa, Mitaka, Tokyo 181-8588, Japan
[4] Institute of Deep Space Sciences, Deep Space Exploration Laboratory, Hefei 230026, People's Republic of China
[5] Department of Astronomy, Kyoto University, Kitashirakawa-Oiwake-cho, Sakyo-ku, Kyoto 606-8502, Japan
[6] Tuorla Observatory, Department of Physics and Astronomy, FI-20014, University of Turku, Finland
[7] Finnish Centre for Astronomy with ESO (FINCA), FI-20014, University of Turku, Finland
[8] Institute of Space Sciences (ICE-CSIC), Campus UAB, Carrer de Can Magrans, s/n, E-08193 Barcelona, Spain
[9] Institut d'Estudis Espacials de Catalunya (IEEC), 08860, Castelldefels (Barcelona), Spain
[10] Department of Physics and Astronomy, Rutgers, The State University of New Jersey, 136 Frelinghuysen Road, Piscataway, NJ 08854, USA
[11] Department of Astronomy, University of Washington, Box 351580, Seattle, WA 98195-1580, USA
[12] McWilliams Center for Cosmology, Department of Physics, Carnegie Mellon University, 5000 Forbes Avenue, Pittsburgh, 15213 PA, USA
[13] State Key Laboratory of Particle Detection and Electronics, University of Science and Technology of China, Hefei 230026, People's Republic of China
[14] National Optical Astronomy Observatory (NSF's National Optical-Infrared Astronomy Research Laboratory), 950 N. Cherry Avenue, Tucson, AZ 85726, USA
[15] Institute of Optics and Electronics, Chinese Academy of Sciences, Chengdu 610209, People's Republic of China
[16] Purple Mountain Observatory, Chinese Academy of Sciences, Nanjing 210023, People's Republic of China
[17] Tsung-Dao Lee Institute and Key Laboratory for Particle Physics, Astrophysics and Cosmology, Ministry of Education, Shanghai Jiao Tong University, Shanghai 201210, People's Republic of China

Received 2025 December 7; revised 2026 February 26; accepted 2026 February 27; published 2026 April 24

Abstract

We present comprehensive photometric and spectroscopic observations of a transitional Type Ia supernova (SN Ia), SN 2024aedt, discovered by the 2.5 m Wide Field Survey Telescope within 1 day of the explosion. Its light curve is characterized by a peak absolute magnitude of $M_B = -18.49 \pm 0.03$ mag and a decline rate of $\Delta m_{15}(B) = 1.53 \pm 0.36$ mag, placing the object on the $\Delta m_{15}(B)$–M_B diagram in the transition region between normal and subluminous SNe Ia. Furthermore, the early color evolution and host galaxy environment of SN 2024aedt underscore its transitional nature, sharing properties with both normal and SN 1991bg–like SNe Ia. Light-curve modeling with `MOSFiT` yields a synthesized ^{56}Ni mass of $0.414 \pm 0.042\,M_\odot$ and a total ejecta mass of $0.548 \pm 0.108\,M_\odot$. A comparison with theoretical models suggests that the evolutionary trend can be broadly explained by both delayed-detonation and double-detonation (DDet) scenarios, while possible early-excess emissions predicted by DDet cannot be identified given the limited detections soon after the SN explosion. Although the overall spectral evolution of SN 2024aedt is similar to that of other transitional SNe Ia, the spectroscopic comparison reveals diversity in the early-phase blue-end features, which becomes more homogeneous at later phases. This result indicates the importance of early-time observations in understanding the origin of SN Ia diversity.

Unified Astronomy Thesaurus concepts: Type Ia supernovae (1728); Observational astronomy (1145); Surveys (1671); Transient detection (1957); Optical astronomy (1776)

Materials only available in the online version of record: machine-readable table

1. Introduction

Type Ia supernovae (SNe Ia) are thermonuclear explosions of carbon–oxygen white dwarfs (WDs). Their extreme luminosity places them among the most energetic events observed in the Universe. Because of the homogeneous photometric properties of a majority of SNe Ia (M. M. Phillips 1993; M. M. Phillips et al. 1999), they serve as standardizable cosmological distance indicators (S. Perlmutter et al. 1997, 1999; A. G. Riess et al. 1998). However, the intrinsic diversity of SNe Ia introduces systematic uncertainties into cosmological measurements by utilizing them as standard candles (M. Vincenzi et al. 2024).

Based on photometric and spectroscopic observations, SNe Ia are classified into several subclasses in addition to the homologous, well-defined "normal" population. SN 1991T–like SNe Ia are characterized by high peak luminosities and broad light curves. Their early-time spectra are dominated by a blue, featureless continuum with strong absorptions of Fe III. While lines of intermediate-mass elements (IMEs) begin to emerge around the time of maximum brightness, they remain weaker than those seen in normal SNe Ia (A. V. Filippenko et al. 1992b;

S. Taubenberger 2017). In contrast, SN 1991bg–like SNe Ia are subluminous and exhibit rapidly declining light curves. Unlike normal SNe Ia, their early spectra are rich in IMEs. However, they transition to a phase dominated by iron-group elements (IGEs) much earlier than normal SNe Ia. This occurs because the line-forming region recedes more rapidly into the IGE-rich core owing to their lower explosion energy. Furthermore, the appearance of a prominent Ti II feature around maximum brightness is a key characteristic of this subclass (A. V. Filippenko et al. 1992a; S. Taubenberger 2017).

Between these two extremes lie several transitional subtypes that bridge the gap between the normal population and the luminous or subluminous categories. For instance, SN 1999aa–like SNe initially resemble SN 1991T–like events but evolve to behave like normal SNe Ia at an earlier phase (K. Krisciunas et al. 2000; G. Garavini et al. 2004; S. Jha et al. 2006b; T. Matheson et al. 2008). SN 1986G–like SNe exhibit peak magnitudes and decline rates intermediate between those of normal and SN 1991bg–like SNe Ia (M. M. Phillips et al. 1987) and are identified by a strong Si II λ5972 line and intermediate-strength Ti II lines. These transitional objects play a key role in investigating whether the different subtypes represent distinct classes of objects arising from different progenitor systems or explosion mechanisms. Apart from these, other peculiar subtypes exist, including the SN 2002es–like SNe Ia, which are subluminous but have evolution rates comparable to normal SNe Ia (M. Ganeshalingam et al. 2012); exceptionally luminous super-Chandrasekhar SNe Ia (SNe Ia-SC; D. Andrew Howell et al. 2006; N. K. Chakradhari et al. 2014); SNe Iax, which are thought to be partial or failed thermonuclear explosions (S. Jha et al. 2006a); and SNe Ia-CSM, which show clear features of interaction with circumstellar material (M. Hamuy et al. 2003; J. M. Silverman et al. 2013). The diversity of the SN Ia population has been further highlighted by recent studies (e.g., D. D. Desai et al. 2024; G. Dimitriadis et al. 2025).

Decades of accumulated observational data have led to the proposal of numerous progenitor scenarios and explosion mechanisms to explain both the common traits and distinct characteristics of SNe Ia. These are broadly divided into two main categories: the single-degenerate (SD) scenario, in which a WD accretes material from a nondegenerate companion (J. Whelan & I. Iben 1973; K. Nomoto 1982), and the double-degenerate (DD) scenario, where the merger of two WDs triggers an explosion (A. V. Tutukov & L. R. Yungelson 1981; I. Iben & A. V. Tutukov 1984; R. F. Webbink 1984).

The mass of the exploding WD can be either near the Chandrasekhar mass ($M_{\rm ch}$) or sub-Chandrasekhar mass (sub-$M_{\rm ch}$), depending on the thermonuclear triggering mechanism. Among Chandrasekhar-mass models, a leading theory is the delayed detonation (DDT), where an initial subsonic deflagration wave transitions into a supersonic detonation, which can explain a large fraction of normal SNe Ia (A. M. Khokhlov 1991). Alongside these, sub-$M_{\rm ch}$ mechanisms were proposed, initially to explain subluminous events. The most studied sub-$M_{\rm ch}$ model is the double-detonation (DDet) mechanism, in which the detonation of a surface helium layer on the WD triggers a subsequent, catastrophic detonation of the underlying carbon–oxygen core. If the helium shell is sufficiently thin, this mechanism can explain the main observational properties of normal SNe Ia, not only subluminous ones. This scenario may show distinct signatures in early-time observations, e.g., strong Ti II absorption and photometric excess, due to radioactive isotopes and IGE synthesized in the outer layer of the ejecta (L. Bildsten et al. 2007; J.-a. Jiang et al. 2017, 2018; K. Maeda et al. 2018).

In this paper, we present a systematic study of SN 2024aedt, a transitional SN Ia. The evolution of its light curves and spectrum and the characteristics of its host galaxy are presented. By comparing these features with other transitional SNe and models, the characterization of this object and its possible origins are discussed. Throughout the work, all magnitudes are reported in the AB system. We adopt a flat ΛCDM cosmology with $H_0 = 67.66$ km s^{-1} Mpc^{-1} and $\Omega_m = 0.30966$ from the Planck 18 results (N. Aghanim et al. 2020).

This paper is organized as follows: In Section 2, the observational data for our target are detailed. Section 3 describes our analysis of the photometric and spectroscopic data, as well as the properties of the host galaxy. In Section 4, we synthesize the results of the previous sections to discuss the similarities between transitional and normal SNe Ia and explore the possible explosion mechanisms. Finally, a summary of our findings is provided in Section 5.

2. Observations and Data Reduction

The Wide Field Survey Telescope[18] (WFST; T. Wang et al. 2023) is a 2.5 m optical telescope featuring a 6.5 deg^2 field of view and high u-band sensitivity. It was jointly built by the University of Science and Technology of China (USTC) and the Purple Mountain Observatory (PMO). This design enables WFST to conduct deep surveys of the northern sky, making it a powerful instrument for exploring the variable Universe and discovering extragalactic transients such as SNe (M. Hu et al. 2022) and tidal disruption events. WFST started a 6 yr WFST transient survey project from 2024 December 14.

SN 2024aedt[19] was officially discovered and publicly reported by the Asteroid Terrestrial-impact Last Alert System (ATLAS; J. Tonry et al. 2024) on UT 2024 December 16 09:00:43 (MJD 60660.376) with $m_o = 18.553 \pm 0.182$. The last nondetection was on UT 2024 December 15 09:53:26 (MJD 60659.412), with a limiting magnitude of $m_o \geqslant 18.51$.

However, the transient had been independently detected at an earlier epoch by WFST on UT 2024 December 14 16:35:02 (MJD 60658.691, i.e., the first night of the WFST formal survey) through the Deep High-cadence *ugr*-band Survey project ("DH*ugr*;" J. Jiang et al. 2026, in preparation), a key project for the formal surveys. The first detection has a g-band magnitude $m_g = 19.59 \pm 0.05$ (corrected for Galactic extinction). The last nondetection was on UT 2024 December 08 16:17:45 (MJD 60652.679), with a 5σ limiting magnitude of $m_g \geqslant 22.43$, as measured from one of the individual images used for stacking the reference image. The primary observing strategy involved daily/hourly cadence 90 s exposures in u, g, and r bands. Standard data processing was implemented through the WFST data pipeline, which is built on a modified version of the Large Synoptic Survey Telescope (LSST) software stack (T. Axelrod et al. 2010; J. Bosch et al. 2018; Ž. Ivezić et al. 2019). More details on WFST data processing can be found in M. Cai et al. (2025) and Z. Xu et al. (2026, in preparation). Team members carried out visual inspections of

[18] https://wfst.ustc.edu.cn
[19] https://www.wis-tns.org/object/2024aedt

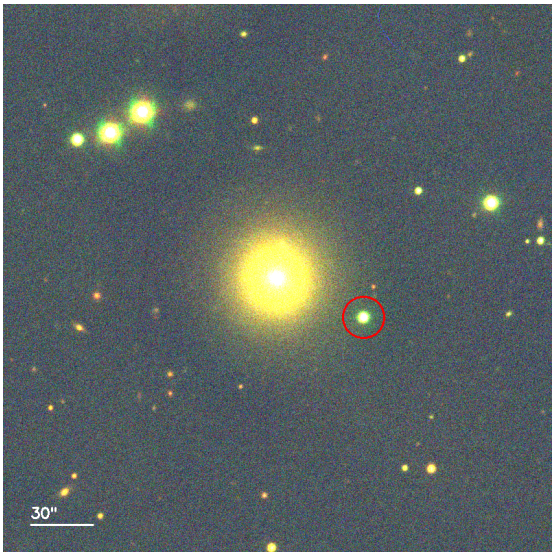

Figure 1. A three-color composite image of SN 2024aedt, observed by WFST on 2024 December 12–25. The image is constructed from *u* (blue), *g* (green), and *r* (red) filter data. The position of the SN is marked by the red circle. A 30″ scale bar is shown in the lower left corner.

all WFST DH*ugr* transient candidates after the real–bogus classification. These inspections were based on specific criteria (including host-center offset, redshift, light-curve morphology, source catalog cross-match, etc.).

2.1. Light Curves

After the discovery of SN 2024aedt, a multiband photometric and spectroscopic follow-up campaign was promptly initiated. The SN was monitored by WFST until 2025 March 07, and the field was revisited by WFST in 2025 August.

The transient is located 46.″49 from the center of its host, the elliptical galaxy UGC 1325 (G. de Vaucouleurs et al. 1991), which has a spectroscopic redshift of $z = 0.018413 \pm 0.000053$ (G. Wegner et al. 2003), as shown in Figure 1. While the NASA/IPAC Extragalactic Database (NED) provides a redshift-independent distance modulus of $\mu_{\rm TF} = 34.70 \pm 0.45$ mag based on the Tully–Fisher relation (G. Theureau et al. 2007), we utilize the redshift-derived distance $\mu_z = 34.59 \pm 0.12$ mag for our primary analysis given its higher precision. The measurement uncertainty of the redshift contributes only ∼0.006 mag to μ, which is negligible. We incorporate an uncertainty of 300 km s^{-1} for the peculiar velocity, corresponding to an uncertainty of ∼0.12 mag in μ. This is in good agreement with the Tully–Fisher distance modulus, with a discrepancy of only 0.24σ.

Figure 2 shows the multiband light curves of SN 2024aedt. Due to the observation schedule for reference image acquisition, no early-time *u*- and *r*-band observations were obtained. By fitting the light curves with a quartic polynomial, the time of maximum brightness for each band is determined to be MJD 60670.71 ± 0.59 (*u* band), MJD 60672.71 ± 1.02 (*g* band), and MJD 60672.85 ± 0.93 (*r* band). Additionally, the *B*-band peak time, as determined by a SALT2 fit (J. Guy et al. 2007), is MJD 60672.71 ± 0.06 (see Section 3.2).

The photometric data were corrected for Milky Way (MW) extinction. The specific extinction values for each band were retrieved from the NASA/IPAC Infrared Science Archive (IRSA) using the `astroquery` package (A. Ginsburg et al. 2019). This service applies the E. L. Fitzpatrick (1999, hereafter F99) extinction law to the E. F. Schlafly & D. P. Finkbeiner (2011) dust map, assuming a default $R_V = 3.1$. The mean Galactic reddening is $E(B - V) = 0.0890 \pm 0.0056$ mag, which corresponds to a *V*-band extinction of $A_V = 0.2824$ mag. Given the large projected distance from its host galaxy, no correction for host galaxy extinction was applied. Given the low redshifts, no *K*-corrections were applied to SN 2024aedt or the comparison sample used in the subsequent analysis.

We also queried the Zwicky Transient Facility (ZTF) Forced Photometry Service (F. J. Masci et al. 2023) and the ATLAS Forced Photometry Service[20] (J. L. Tonry et al. 2018; K. W. Smith et al. 2020; L. Shingles et al. 2021) to obtain supplementary data. Following the official guidelines, these data were processed and corrected for MW extinction and redshift using the same procedure described previously.

Late-time photometric follow-up observations were conducted using telescopes from the Las Cumbres Observatory Global Telescope Network (LCOGT; T. M. Brown et al. 2013). The data processing pipeline began with background subtraction on individual frames using `SWarp` (E. Bertin et al. 2002). Subsequently, `SExtractor` (E. Bertin & S. Arnouts 1996) was employed to detect sources and perform astrometric calibration against the Pan-STARRS DR1 catalog (K. C. Chambers et al. 2016; H. A. Flewelling et al. 2020). This allowed for the calculation of the photometric zero-point for each frame, which was determined via linear regression after a 2σ clipping process and normalized to a reference magnitude of 29. Images in the same band taken on the same night were then coadded. The zero-point of the stacked image was recalculated to ensure consistency. Finally, aperture photometry was performed at the SN position using `Photutils` (L. Bradley et al. 2024). An aperture with a diameter of 5 times the full width at half maximum (FWHM) was used, where the FWHM for each stacked image was measured using `SExtractor`. Some images suffer from fringe artifacts. The correction procedure is described in Appendix A.

It should be noted that the photometric procedures vary across the different surveys. While external data from ZTF and ATLAS utilize their respective automated template-subtraction pipelines, the photometry for WFST and LCO was performed using forced photometry on the science images. For WFST, this approach was chosen because the transient was already present in the data used to construct the *r*-band reference images; forced photometry also allowed us to retrieve the flux during the reference-building period. Furthermore, given the substantial spatial offset of the SN from the host galaxy, the background contribution from the host galaxy at the transient's location is negligible. We also note that, despite the differences in filter transmission profiles across these facilities, the resulting light curves show consistent evolution, with data points from different telescopes agreeing within approximately 1σ uncertainties.

2.2. Color Evolution

Figure 3 presents the $u - g$ and $g - r$ color evolution of SN 2024aedt. The color indices were calculated from nightly binned WFST photometry, and the phase is measured in days

[20] https://fallingstar-data.com/forcedphot/

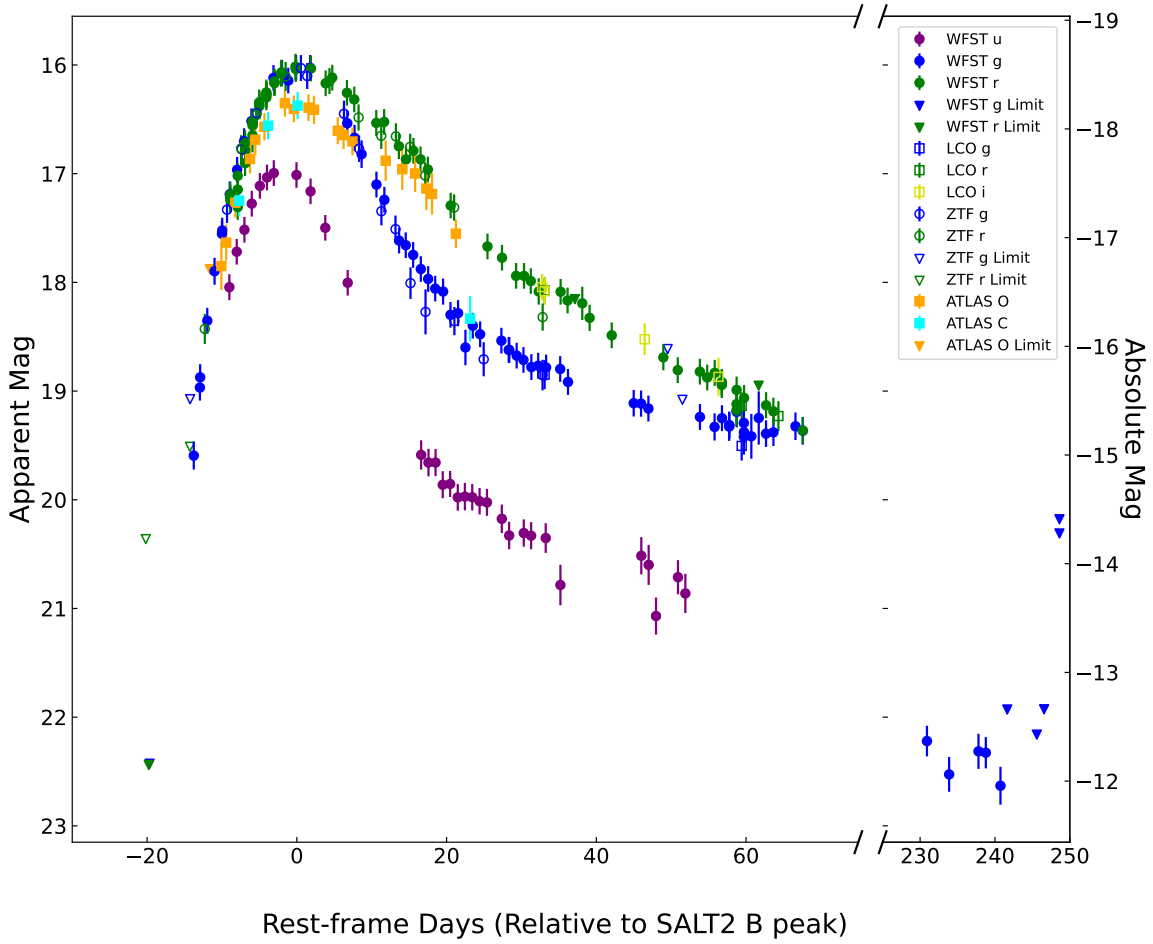

Figure 2. Multiband light curves of SN 2024aedt. The photometry for each band is color-coded as shown in the legend. Triangles denote 5σ upper limits.

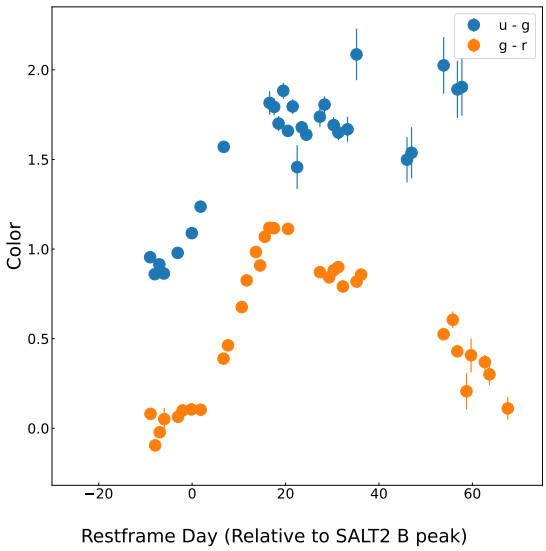

Figure 3. The $u - g$ and $g - r$ color evolution of SN 2024aedt, calculated from nightly binned WFST photometry.

relative to the time of B-band maximum. The $u - g$ color begins at approximately 1.0 mag at a phase of -9 days, becomes slightly bluer, and then steadily reddens to a peak around $+17$ days. The $g - r$ color starts at a value of about 0.0 mag at -9 days and continuously reddens, reaching a peak of approximately 1.12 mag around $+16$ days.

2.3. Spectroscopy

We obtain three spectra of SN 2024aedt using the Kitt Peak Ohio State Multi-Object Spectrograph (KOSMOS) on the 3.5 m Astrophysical Research Consortium (ARC) Telescope at Apache Point Observatory (APO). KOSMOS is a medium-dispersion spectrograph (resolving power up to 2600). Our observations, using the center slit, cover the wavelength ranges 3800–6600 Å (blue) and 5600–9400 Å (red). The observations were conducted on UT 2024 December 18, 2024 December 20, 2025 January 18, and 2025 January 22. The raw data are reduced using the `PyKOSMOS` (J. Davenport 2021) pipeline. The resulting spectra are then corrected for MW extinction using the model of E. L. Fitzpatrick & D. Massa (2007) via the `extinction` package and subsequently transformed to the rest frame. Although no discernible features can be extracted from the earliest KOSMOS spectrum, the other three were successful. One spectrum was also obtained on 2025 January 12 using the Alhambra Faint Object Spectrograph and Camera (ALFOSC) on the Nordic Optical Telescope (NOT; A. A. Djupvik & J. Andersen 2010), with a setup (Grism #4, $1\farcs0$ slit) that provided a wavelength range of 3200–9600 Å and a resolution of $R = 360$.

In addition to our own observations, a publicly available spectrum from the Transient Name Server (TNS) is included in analysis. This spectrum was taken by the POISE group with the Magellan-Baade/IMACS instrument approximately 1 day

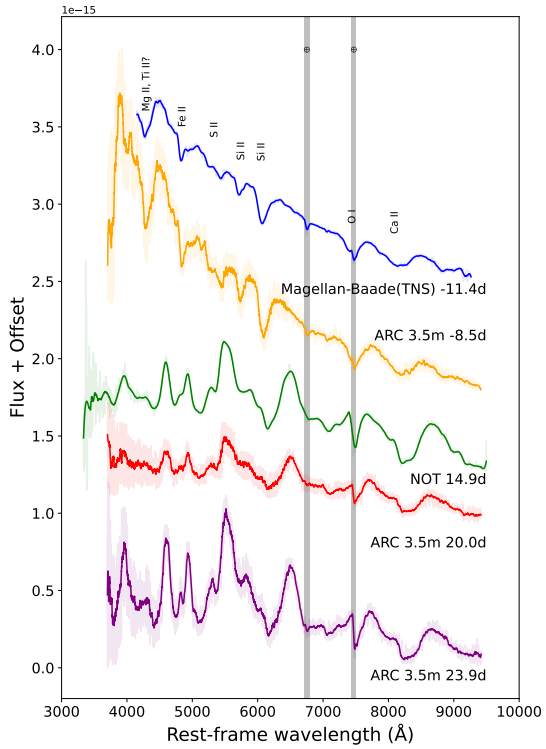

Figure 4. Spectra of SN 2024aedt from multiple epochs and instruments. For display purposes, an arbitrary offset has been applied to the flux of each spectrum. The original data are shown as faint lines, while the solid lines are smoothed versions using a Savitzky–Golay filter (A. Savitzky & M. J. E. Golay 1964). Shaded regions mark the locations of telluric absorption.

before our first KOSMOS observation (N. Morrell et al. 2024). The full spectroscopic sequence is presented in Figure 4.

The premaximum spectra show prominent features characteristic of a normal SN Ia before maximum light. These include Si II λ5972, Si II λ6355, the S II "W" trough, O I λ7774, and the Ca II near-infrared triplet. The feature around 4820 Å is identified as Fe II, while the absorption near 4285 Å is a blend of Mg II and Ti II. In the post-maximum spectra, Ca II and Si II lines remain visible. A blended absorption feature around 5750 Å is identified as Na I D, and the 4500–5500 Å region is dominated by Fe II lines. Our final spectrum, taken at a phase of +24.0 days relative to B-band maximum, indicates that the SN had not yet entered the nebular phase.

3. Results

3.1. Explosion Time

To determine the explosion time (t_0) and characterize the early light curve, we fit the rising-phase photometry with the following power-law function:

$$f(t) = A(t - t_0)^{\alpha}. \quad (1)$$

Following the methodology described in R. P. Olling et al. (2015), only photometric points with a flux below 40% of the peak were included in the fit. The fit was performed in the rest-frame time, presented in Figure 5, and yields the following best-fit parameters: an amplitude of $A = 4545.557 \pm 1314.776$ nJy, a power-law exponent of $\alpha = 2.266 \pm 0.105$, and a time of first light of $t_0 = \text{MJD } 60655.603 \pm 0.263$.

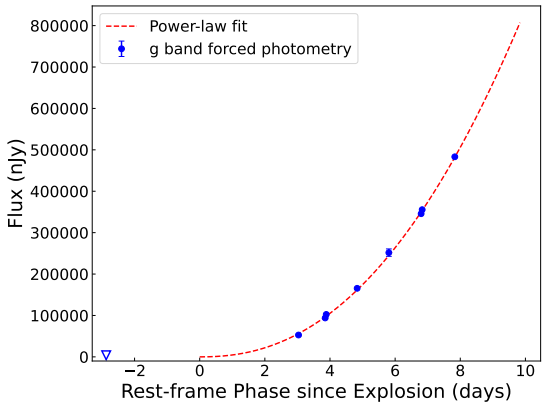

Figure 5. Power-law fit to the early g-band light curve. The fitting procedure and results are described in Section 3.1.

The resulting exponent, $\alpha = 2.266$, is consistent with the predictions of an expanding fireball model for an SN shortly after explosion (A. G. Riess et al. 1999), also consistent with the result from A. A. Miller et al. (2020) of $2.08^{+0.15}_{-0.13}$ around 1.02σ. While the smooth power law provides an excellent fit to the detected early-time data, we note that the gap between the last nondetection and the inferred explosion time means that a short-lived early flux excess—potentially arising from multiple possibilities (D. Kasen et al. 2009; J.-a. Jiang et al. 2017, 2018, 2021)—cannot be definitively ruled out.

3.2. SALT2 and SNooPy Fitting

We fit WFST g- and r-band light curves using the `SALT2` model (J. Guy et al. 2007) implemented in the `snfit` (v2.4.2) package. The best fit yields a peak absolute B-band magnitude of $M_B = -18.49 \pm 0.03$ mag, occurring at MJD 60672.711 ± 0.058. The light-curve shape parameters are $x_1 = -2.253 \pm 0.043$ and $c = 0.001 \pm 0.028$. A decline rate parameter of $\Delta m_{15}(B) = 1.53 \pm 0.36$ mag is calculated using the relation from Section 5 of J. Guy et al. (2007). To cross-validate this result, we performed a direct fourth-order polynomial fit to the g-band photometry around the peak, yielding $\Delta m_{15}(g) = 1.614 \pm 0.003$ mag and $M_g = -18.53 \pm 0.06$ mag. The error was derived from Monte Carlo simulations. The result of `SALT2` fitting is plotted on the $\Delta m_{15}(B)$–M_B diagram in the top panel of Figure 6, along with a comparison sample from M. Hicken et al. (2009; excluding objects at $z < 0.01$) and other transitional events. As shown in the figure, SN 2024aedt lies at the faint, fast-declining end of the distribution, below the canonical Phillips relation.

A comparison with the SN Ia population in S. Taubenberger (2017, see their Figure 1) places SN 2024aedt on the boundary between normal SNe Ia and the subluminous SN 1991bg–like class. It is slightly more luminous and slower evolving than the prototypical transitional object, SN 1986G (M. M. Phillips et al. 1987; S. Taubenberger et al. 2008). Based on these characteristics, SN 2024aedt is classified as a subluminous transitional SN Ia of the SN 1986G–like subclass.

We also fitted the light curves with `SNooPy` (C. R. Burns et al. 2011) to determine the color stretch parameter, s_{BV} (C. R. Burns et al. 2014). Using the WFST ugr data, this fit yields $s_{BV} = 0.574$. This value is plotted as a red dotted line,

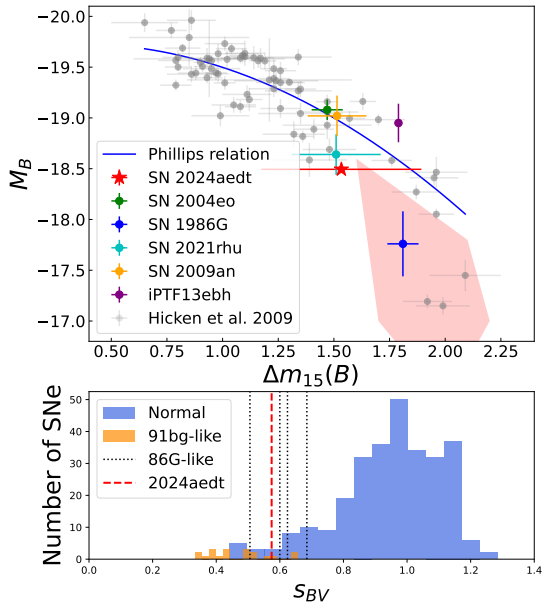

Figure 6. Top panel: the $\Delta m_{15}(B)$–M_B diagram (Phillips relation) for SN 2024aedt and the M. Hicken et al. (2009) comparison sample (excluding objects at $z < 0.01$). SN 2024aedt is indicated by the red star; see Section 3.2 for details. The blue line represents the Phillips relation (M. M. Phillips et al. 1999). The "91bg-like" region from S. Taubenberger (2017) is shown in red. (It should be noted that this region is not strictly "91bg-like" but also includes part of the parameter space for transitional SNe.) Details of the transitional sample can be found in Section 3.5. Bottom panel: histogram of the s_{BV} distribution for SN 2024aedt and the S. A. Uddin et al. (2024) sample. SN 2024aedt is indicated by a red dashed line, and SN 1986G–like objects from the S. A. Uddin et al. (2024) sample are marked by black dotted lines.

along with the sample from S. A. Uddin et al. (2024), in the bottom panel of Figure 6. SN 2024aedt, together with other SN 1986G–like events, falls in the region between the SN 1991bg–like and normal populations.

3.3. Light-curve Fitting

We modeled the light curve of SN 2024aedt using Modular Open-Source Fitter for Transients (`MOSFiT`; J. Guillochon et al. 2018). This Python-based package employs Monte Carlo methods to generate ensembles of semianalytical light-curve fits and derive Bayesian posterior distributions for model parameters. For this work, the `ia` model (D. K. Nadyozhin 1994) is applied to the *ugr*-band photometric data at phases earlier than +40 days.

The resulting model realizations are shown against the data in Figure 7, while the parameter posterior distributions are presented in Figure B1. The model provides a good overall fit, although the observed *g*-band data begin to deviate slightly from the best-fit model after a phase of +35 days. From the posterior distributions, we derive a synthesized ^{56}Ni mass of $0.414 \pm 0.042\,M_\odot$ and a total ejecta mass of $0.548 \pm 0.108\,M_\odot$. The explosion time given by `MOSFiT` has a gap of around 1.5 days with the power-law fitting result. This might be because `MOSFiT` is constrained by the overall light-curve morphology and diffusion physics, whereas the power-law fit only provides the time of "first light."

3.4. Comparison Sample of Light Curves and Spectra

We compiled a sample of transitional SNe Ia from the literature for comparison, including SN 2021rhu

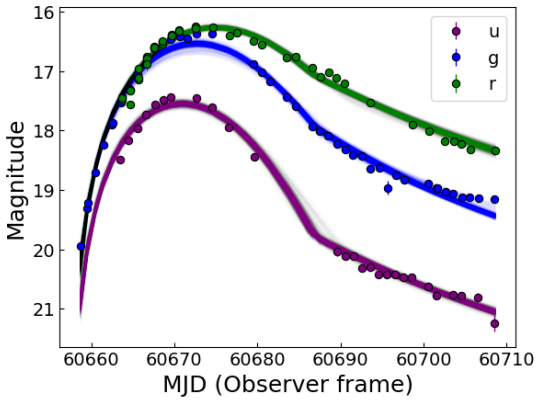

Figure 7. The observed *ugr*-band photometry (filled circles) overlaid with a representative sample of model light-curve realizations (solid lines) from the `MOSFiT` posterior distribution.

(L. Harvey et al. 2023), SN 1986G (M. M. Phillips et al. 1987), SN 1998bp (S. Jha 2002), SN 2003gs (K. Krisciunas et al. 2009), SN 2007on (C. Gall et al. 2018), SN 2011iv (C. Gall et al. 2018), iPTF13ebh (E. Y. Hsiao et al. 2015), SN 2003hv (G. Leloudas et al. 2009), SN 2004eo (C. Contreras et al. 2010; A. Pastorello et al. 2007), SN 2005am (C. Contreras et al. 2010), SN 2009an (D. K. Sahu et al. 2013), SN 2012ht (C. R. Burns et al. 2018), and SN 2015bp (S. D. Wyatt et al. 2021).

For broader comparison, examples of normal and SN 1991bg–like SNe Ia are also included. The photometric data for these objects were obtained from the Open Supernova Catalog (J. Guillochon et al. 2017). This part of the sample includes the normal SNe Ia SN 2015F (M. L. Graham et al. 2017; C. R. Burns et al. 2018) and SN 2011fe (R. E. Firth et al. 2015; M. L. Graham et al. 2017) and the SN 1991bg–like SN 2005bl (C. Contreras et al. 2010).

The data for the comparison sample were processed as follows. Unless otherwise specified, the distance modulus for each SN was adopted from its primary reference cited above. For the following objects, however, the distance moduli were sourced from different papers: SN 1998bp (M. Ganeshalingam et al. 2013), SN 2004eo and SN 2005am (P. Hoeflich et al. 2017), SN 2015F (R. Cartier et al. 2017), SN 2005bl (W. M. Wood-Vasey et al. 2008), and SN 2011fe (S. Dhawan et al. 2016). For SN 1986G, which suffers from significant host galaxy extinction, we adopted the host extinction values (A_B and $E(B-V)$) directly from M. M. Phillips et al. (1987). For the remaining objects, photometry was corrected for MW extinction using the procedure described previously, with the exception of SN 2004eo, SN 2005am, and SN 2005bl, for which precorrected data were used.

3.4.1. Multiband Photometric Comparison

The absolute magnitude light curves of the full comparison sample are presented in Figure 8. For clarity, data obtained from various facilities are grouped by their respective filters (*u*, *g*, and *r*). The figure shows a clear separation based on SN subtype: normal SNe Ia populate the luminous, slow-evolving region at the top of the plot, while the SN 1991bg–like SN 2005bl occupies the subluminous, fast-evolving region. The transitional SNe Ia are distributed between these two extremes. The light-curve evolution of SN 2024aedt is consistent with this transitional group.

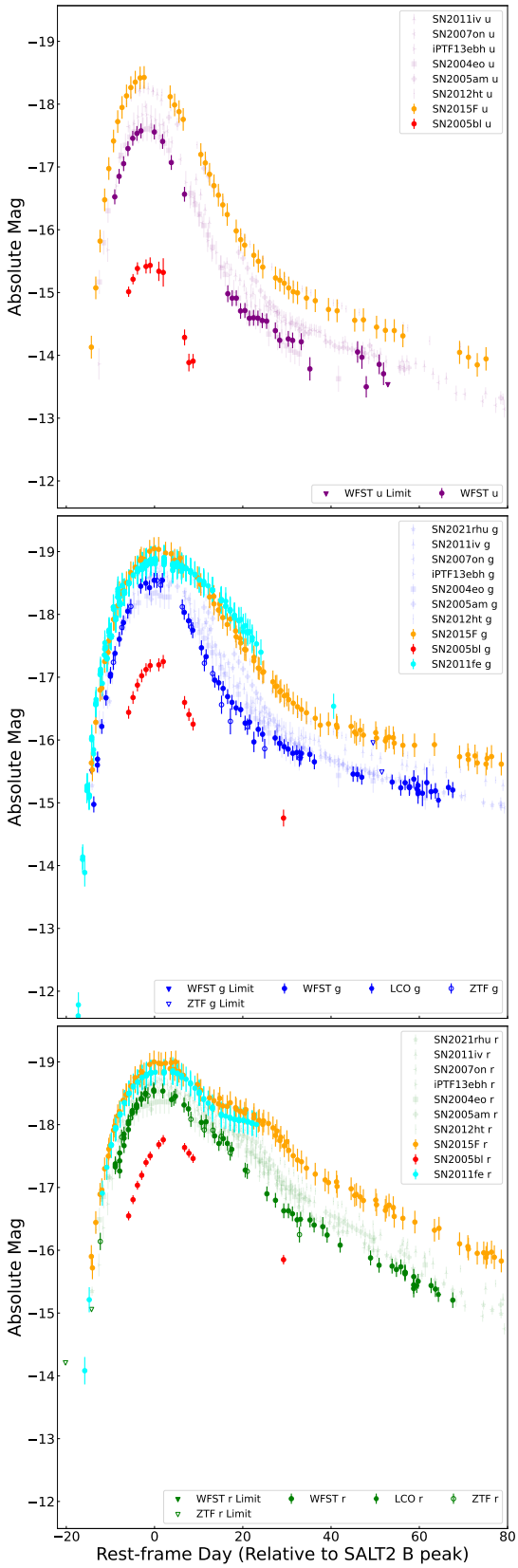

Figure 8. Light-curve comparison for SN 2024aedt and other SNe Ia. Data are coded by color and opacity as follows: SN 2024aedt (filled purple, blue, and green points), a transitional SN Ia sample (semitransparent points), normal SNe Ia SN 2011fe (cyan) and SN 2015F (orange), and the SN 1991bg–like SN 2005bl (red).

A feature of SN 2024aedt is the weak secondary maximum in the redder bands. In the rest frame, the *r*-band light curve between +15 and +20 days shows a shoulder that is much less prominent than those seen in normal SNe Ia. This is thought to be a consequence of a smaller synthesized mass of IGEs compared to normal events, as well as the IGE distribution and metallicity (D. Kasen 2006; M. Deckers et al. 2025).

The comparison also highlights the diversity within the transitional class itself, which is most apparent in the bluer bands. The *u* band, in particular, reveals the largest separation between the SN 1991bg–like SN 2005bl and the transitional events. The transitional SNe themselves exhibit a peak magnitude spread of up to 1 mag in this band, while the dispersion is smaller in the *g* and *r* bands. However, we note that since no host galaxy extinction correction was applied (with the exception of the heavily reddened SN 1986G), this observed dispersion—particularly in the bluer filters—may be partially influenced by extrinsic dust reddening rather than intrinsic diversity alone.

Finally, the absolute peak magnitudes for some objects in the comparison sample should be treated with caution, as they may be uncertain. This is due to the significant uncertainties in the distance moduli for some nearby SNe; values available in public databases like NED can have a large scatter, which directly impacts the calculated absolute magnitudes. For SN 2024aedt, the impact of a typical peculiar velocity on its redshift-derived distance modulus is estimated to be at most 0.1–0.2 mag. This level of uncertainty is insufficient to alter its classification as a transitional object.

Figure 9 shows the $u - g$ and $g - r$ color evolution for the full comparison sample. As with the light curves, a clear separation between the subtypes is evident, with the transitional SNe Ia occupying a region between the normal and the SN 1991bg–like populations. The SN 1991bg–like SN 2005bl exhibits the fastest color evolution, cooling much more rapidly than any other object in the sample. Due to the lack of late-time photometric coverage for SN 2005bl, we supplemented our comparison with the SN 1991bg–like object ZTF19aahjhoy (SN 2019arb) from the ZTF DR2 archive (M. Rigault et al. 2025). Using the *g*-band peak as the reference epoch, the $g - r$ color evolution of SN 2019arb shows the rapid cooling seen in SN 2005bl during the early phases, reaching a red color peak before evolving blueward at a rate consistent with the overall sample.

The normal SNe Ia also show diverse behavior. SN 2011fe, a prototypical normal event, displays a particularly complex $g - r$ evolution: it first rapidly becomes bluer until a phase of approximately −12 days, after which its color changes much more slowly for the next 15 days. This is followed by a brief period of reddening, a subsequent 10-day blueing trend, and finally a rapid evolution toward redder colors. Interestingly, the normal SN 2015F, reported as a slightly subluminous SN Ia (R. Cartier et al. 2017), follows the general trend of the transitional events, though it remains in a parameter space closer to SN 2011fe.

Within this context, SN 2024aedt is situated on the faster-evolving side of the transitional population. This rapid color evolution corresponds to its relatively subluminous nature as observed in the light-curve comparison.

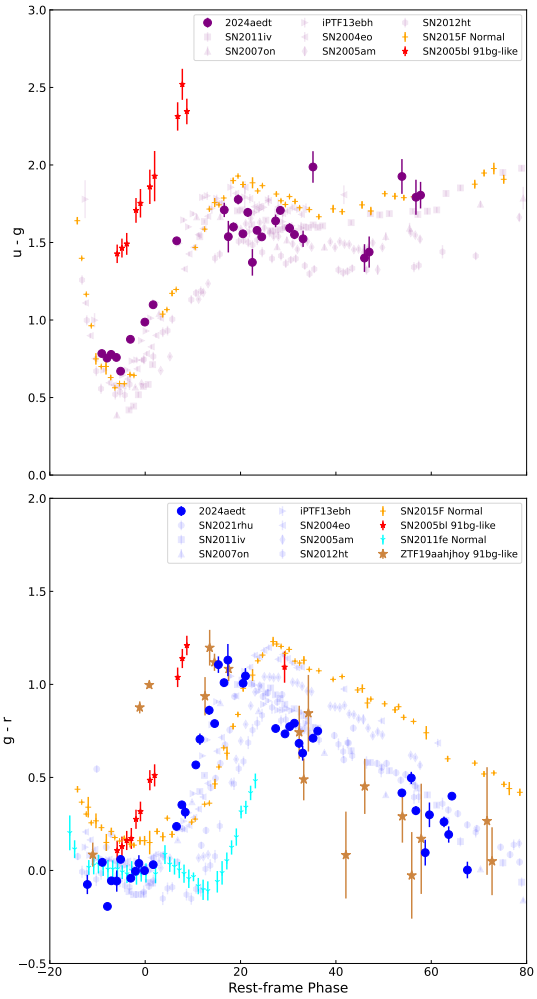

Figure 9. Color evolution comparison for SN 2024aedt and other SNe Ia. The data are coded by color and opacity as follows: SN 2024aedt (filled purple and blue points), the transitional SN Ia sample (semitransparent points), the normal SN 2011fe (cyan), the slightly subluminous normal SN 2015F (orange), and the SN 1991bg–like SN 2005bl (red) and ZTF19aahjhoy (peru).

3.4.2. Spectra for Comparison

To perform a spectral comparison, we collected all available spectra for our comparison sample from the Weizmann Interactive Supernova Data Repository[21] (WISeREP; O. Yaron & A. Gal-Yam 2012). The redshift correction status of each spectrum was verified by examining the wavelengths of telluric absorption features. After verification, the spectra were corrected for redshift and MW extinction as needed, using the procedure described previously. For each SN 2024aedt observation, the comparison spectrum with the closest phase within a ±2-day window was selected from each source in the sample. The resulting spectral comparisons are presented in Figures 10–12.

In the premaximum epochs, the ejecta velocity of SN 2024aedt, measured from the absorption minimum of the Si II λ6355 line, is similar to those of the transitional SN 2021rhu and SN 2012ht and slightly higher than those of the transitional SN 2004eo and the normal SN 2011fe. Although SN 2021rhu exhibits a similar photometric evolution to SN 2024aedt (Figure 8), there is significant diversity in the features between 4500 and 5000 Å. This combination of overall similarity and diversity in the blue-end features persists into the post-maximum spectra. However, as the SNe evolve, their spectral features become more homogeneous, a trend that is particularly evident in the latest-phase comparison.

This evolutionary trend suggests that early-time spectra are more sensitive probes of the explosion physics than late-time spectra. The initial diversity may be due to differences in the chemical composition or physical state of the outer ejecta, which are in turn influenced by progenitor properties and explosion mechanisms (e.g., J.-a. Jiang et al. 2017).

We measured the pseudo−equivalent widths (pEWs) and velocities of the silicon lines (Si II $\lambda\lambda$5972 and 6355) in the premaximum spectra using a direct interactive procedure. Each spectrum was first corrected for MW extinction and redshift and then smoothed using a Savitzky–Golay filter (A. Savitzky & M. J. E. Golay 1964). A pseudocontinuum was subsequently defined by interpolating between interactively selected local maxima, and the absorption features were then fitted with Gaussian profiles to measure their properties on the raw spectrum. The fitting region and initial guesses for the Gaussian parameters were also selected interactively. To quantify the uncertainties inherent in this interactive process, a Monte Carlo simulation with 10,000 trials is performed. In each trial, the position of every manually selected point (e.g., continuum anchors, fitting boundaries) was randomly perturbed, assuming a characteristic uncertainty of 20 Å for each selection. The final measurements are taken as the median of the resulting distributions, with the 16th and 84th percentiles adopted as the lower and upper 1σ uncertainties, respectively. Then, we manually check the results and remove the failed ones.

In Figure 13, the evolutionary track of SN 2024aedt is plotted on the Branch diagram, which shows pEW(Si II λ5972) versus pEW(Si II λ6355) (D. Branch et al. 2006). The background comparison data are from S. Blondin et al. (2012). It is important to note that the Branch diagram is conventionally plotted using measurements taken at the time of maximum brightness. Since our observations do not cover this specific epoch, the end point of our measured track does not represent the SN's final classification position on this diagram. Nevertheless, the premaximum track shows that the transitional SNe—SN 2024aedt, SN 2004eo, and SN 2012ht—are distributed across the "cool" (CL) region, in good agreement with the results of M. Ogawa et al. (2023) and U. Burgaz et al. (2025). In contrast, the normal SN 2011fe rapidly evolves from the edge of the CL region toward the "core-normal" (CN) region, where it eventually resides at maximum light (R. Pereira et al. 2013).

The evolution of the pEWs and line velocities is presented in Figure 14. The SNe in our sample exhibit diverse pEW evolution. For the normal SN 2011fe, the pEW of Si II λ6355 declines significantly over approximately 4 days, consistent with the findings of X. Zhao et al. (2020), while the other SNe show no clear trend for this feature. In contrast, for the Si II λ5972 line, both SN 2024aedt and SN 2004eo show a slight increase in pEW; for the Si II λ6355 line, however, this increasing trend is only apparent for SN 2024aedt. Compared with the measurements of the CN and CL subtypes from the first phase of the Carnegie Supernova Project (CSP-I; G. Folatelli et al. 2013), our results are consistent with the distribution and evolutionary trends reported in their work for the Si lines of

[21] https://www.wiserep.org

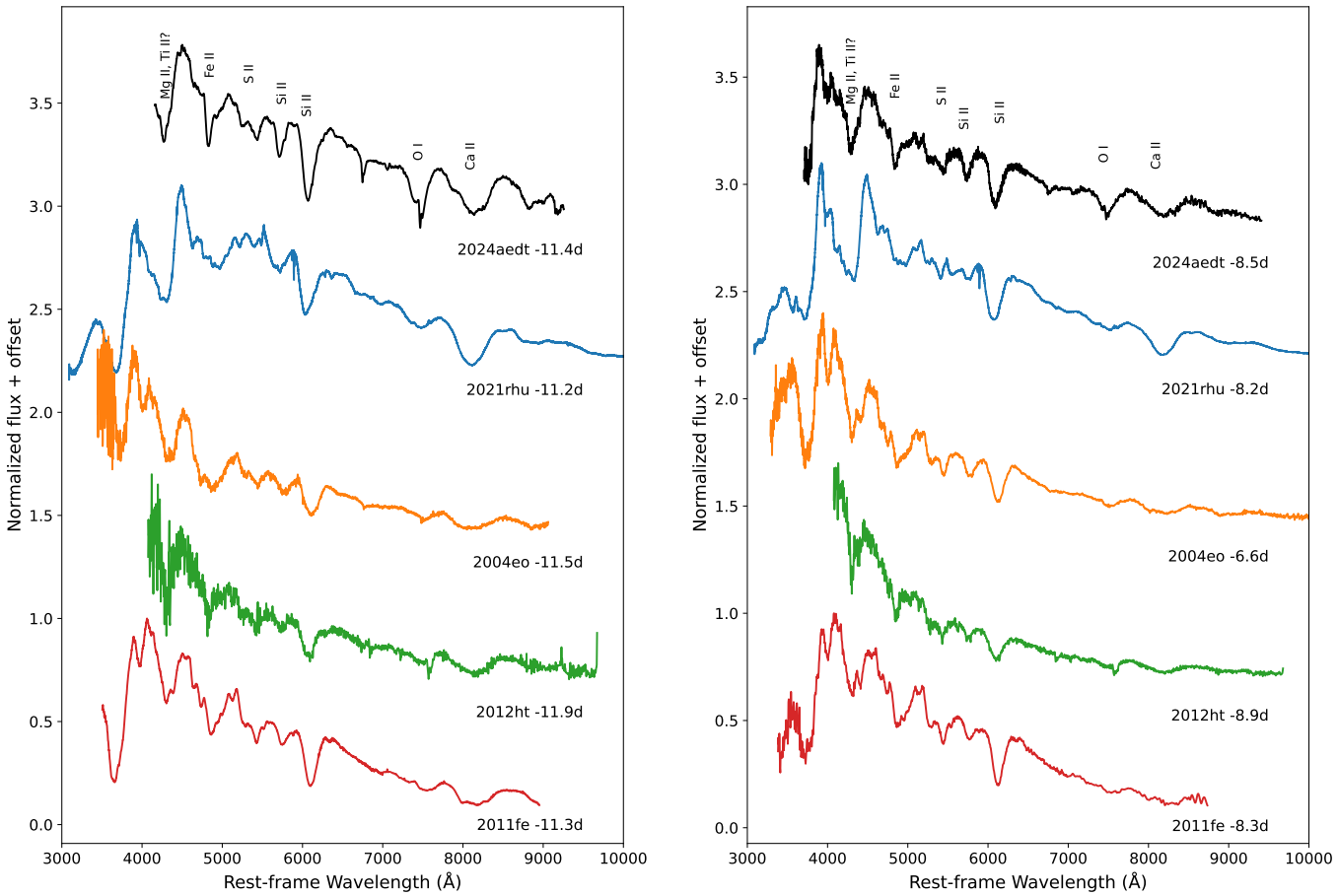

Figure 10. Comparison of spectra at similar phases. The spectrum of SN 2024aedt is shown in black, plotted against other SNe Ia from the comparison sample. Each spectrum is normalized and vertically offset for clarity. See Section 3.4.2 for details.

both normal and transitional events. Furthermore, it should be noted that the pEW values presented here may have significant uncertainties, which can arise from the subjective definition of the pseudocontinuum and potential light contamination from the host galaxy, especially given our limited number of spectra.

The line velocities, measured from the Si II λ6355 feature, all show a clear decreasing trend over time. This behavior is in good agreement with the general trend for SNe Ia presented in J. M. Silverman et al. (2012) and G. Folatelli et al. (2013). The velocity values for SN 2024aedt lie well within the range spanned by the comparison sample.

3.5. Host Galaxy

We obtained multiband photometry for the host galaxy, UGC 1325, using the `hostphot` package (T. E. Müller-Bravo & L. Galbany 2022). The photometric measurements were compiled from several surveys, including the Sloan Digital Sky Surve (SDSS, *ugriz*; Abdurro'uf et al. 2022), the Wide-field Infrared Survey Explorer (WISE, W1–W3; E. L. Wright et al. 2010), the Two Micron All Sky Survey (2MASS, *J*, *H*, K_s; M. F. Skrutskie et al. 2006), and the Galaxy Evolution Explorer (GALEX, NUV; D. C. Martin et al. 2005). The complete photometric dataset is presented in Table 1.

The spectral energy distribution (SED) of the host galaxy was then modeled using `CIGALE` (M. Boquien et al. 2019). The model was constructed using the simple stellar population (SSP) models of G. Bruzual & S. Charlot (2003) with a Chabrier initial mass function (G. Chabrier 2003), a modified dust attenuation law from S. Charlot & S. M. Fall (2000), and dust emission templates from B. T. Draine et al. (2014). An initial fit revealed a flux excess around 2 μm, which was significantly improved by the inclusion of an active galactic nucleus (AGN) component based on the models of M. Stalevski et al. (2012) and M. Stalevski et al. (2016). The final best-fit SED is shown in Figure 15. The fitting result indicates that UGC 1325 is a massive, quiescent elliptical galaxy with a stellar mass of $M_\star \approx 3.914 \times 10^{11}\, M_\odot$. The SFH shows that the galaxy is ancient, having begun forming stars approximately 13 Gyr ago over a timescale of $\tau_{\rm main} \approx 500$ Myr. This resulted in a stellar population with a mass-weighted age of 12 Gyr and a high metallicity ($Z = 0.050$). The galaxy is now fully quenched, with a star formation rate averaged over the past 100 Myr of only $0.024 \pm 0.054\, M_\odot\, {\rm yr}^{-1}$. The galaxy's IR emission is dominated by an obscured AGN, which contributes 70% of its total IR luminosity.

4. Discussion

4.1. SN 2024aedt as a Link between the Normal and Subluminous Classes

The `SALT2` fit yields a peak absolute magnitude of $M_B = -18.49 \pm 0.03$ mag and a decline rate of $\Delta m_{15}(B) = 1.53 \pm 0.36$ mag, placing SN 2024aedt in the transitional region between normal and SN 1991bg–like SNe Ia. This is also evident from the distribution of s_{bv} in the bottom panel of Figure 6. The light curves are consistent with

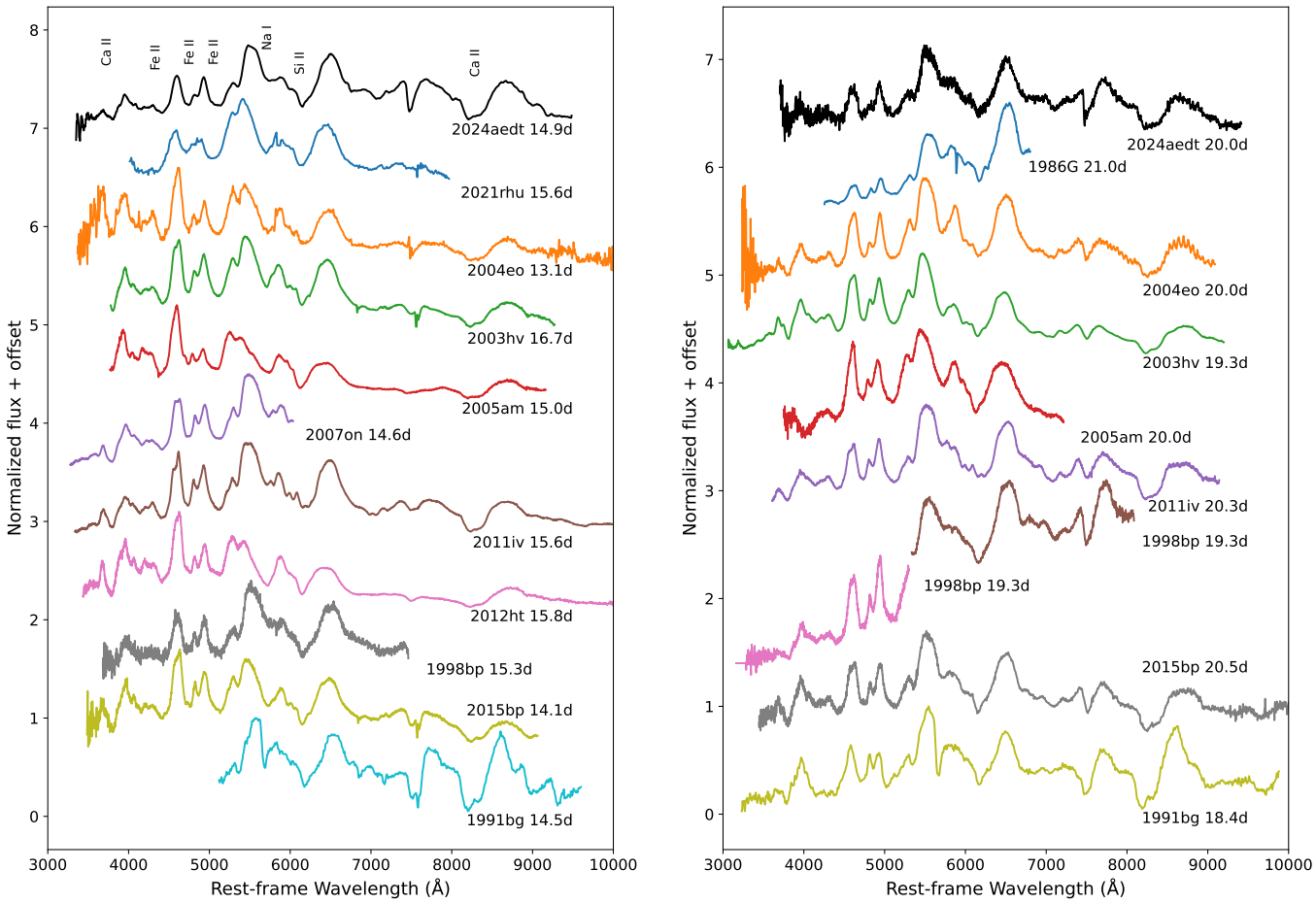

Figure 11. Spectral comparison of SN 2024aedt (continued). The plotting conventions are the same as in the previous figure.

other transitional events, lying on the subluminous, fast-evolving end of the distribution. A subtle secondary maximum is observed in r band, the strength of which appears related to the peak magnitude, consistent with the findings of M. Deckers et al. (2025). This consistency is also reflected in the color evolution, which shows high similarity to other transitional events. The `MOSFiT` analysis yields a synthesized ^{56}Ni mass of 0.414 $M_{\odot}$, a value intermediate between those of normal and SN 1991bg–like SNe Ia.

Following the method of W. Wu et al. (2025), we calculated the rest-frame rise time from -13 mag to the peak in the g band to be $\Delta t_{m(-13)} = 14.834$ days. This result places SN 2024aedt in the lower left corner of both panels in their Figure 2 (see Figure 16). In the $M_{B,\max}$ versus $\Delta t_{m(-13)}$ plane, SN 2024aedt appears separate from the normal SN Ia population, due to the selection criteria (i.e., the limitation to spectroscopically normal SNe Ia at $z < 0.03$ with early-phase detections, which removes most fast-evolving transitional events). In the $\Delta m_{15}(B)$ versus $\Delta t_{m(-13)}$ plane, SN 2024aedt seems to follow the linear trend of the normal group and is close to the normal SN Ia SN 2019ein (M. Kawabata et al. 2020; G. Xi et al. 2022). This similarity is further supported by its early-time color evolution. The early colors of normal SNe Ia like SN 2011fe and SN 2015F show a trend similar to transitional events until the secondary maximum in SN 2011fe's light curve becomes dominant, whereas the SN 1991bg–like SN 2005bl shows a much more rapid reddening. However, a closer look at the color diagram reveals that an evolutionary trend is still present. If the colors of some sources with faster-evolving light curves were included, this trend would likely be more pronounced, which also reflects the diversity within the transitional group. Furthermore, host properties of our compiled transitional sample (Table 2) suggest no significant preference for elliptical hosts, which are typical for SN 1991bg–like SNe Ia (S. González-Gaitán et al. 2011; R. Senzel et al. 2025). This underscores the diversity and highlights the intermediate nature of the class, which shares properties with both the normal and SN 1991bg–like populations. Therefore, the analysis of its photometric properties and derived physical parameters robustly highlights the transitional characteristics of SN 2024aedt.

4.2. Transitional SN 2024aedt: DDT or DDet Origin?

We constructed the pseudobolometric light curve using the `superbol` code (M. Nicholl 2018). The fit incorporated our well-sampled u-, g-, and r-band data, as these bands provide the best coverage, corresponding to a wavelength range of approximately 3000–7000 Å.[22] We compared the result with theoretical models from the Heidelberg Supernova Model Archive (HESMA; M. Kromer et al. 2017), considering two main scenarios: DDT and DDet. We use the angle-averaged bolometric light-curve data directly as provided in HESMA.

[22] Due to strong absorption features and the limited passbands used, bolometric parameters derived via blackbody approximation should be treated as qualitative guides.

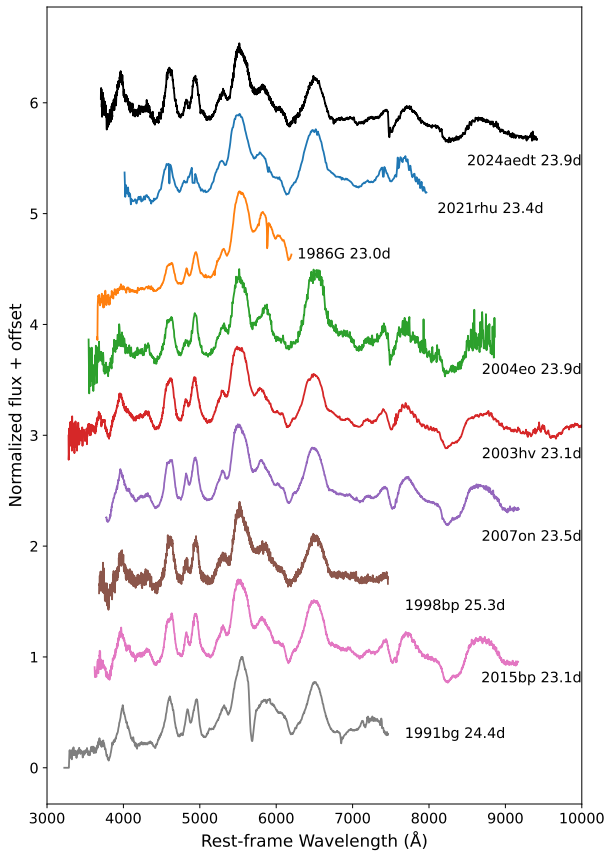

Figure 12. Spectral comparison of SN 2024aedt (continued). The plotting conventions are the same as in the previous figure.

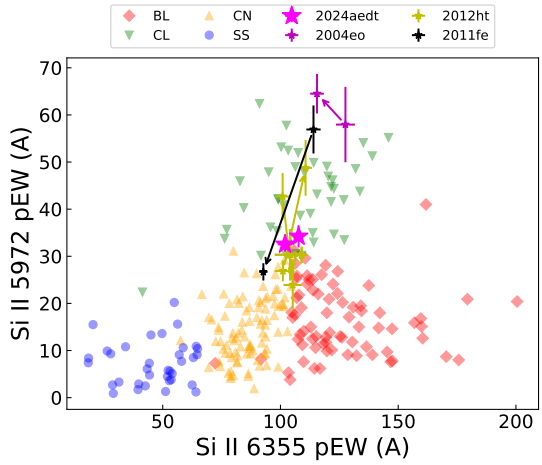

Figure 13. Early-time evolutionary tracks on the Branch diagram. The track for SN 2024aedt is shown in magenta, plotted alongside the normal SN 2011fe (black) and two other transitional SNe Ia. See Section 3.4.2 for a detailed description.

We plotted and inspected the full suite of available models, most of which showed significant discrepancies with SN 2024aedt; only two models show a good match to our data (Figure 17). The first is a near-$M_{\rm ch}$ DDT model (`ddt_2013_n200`; I. R. Seitenzahl et al. 2013; S. A. Sim et al. 2013) from a nonrotating WD with 200 ignition kernels, which produces 0.41 $M_\odot$ of ^{56}Ni and a kinetic energy of 1.34×10^{51} erg. The second is a sub-$M_{\rm ch}$ DDet model (`doubledet_2021_m0905_1`; S. Gronow et al. 2021) with a 0.899 $M_\odot$ core and a 0.053 $M_\odot$ helium shell, synthesizing 0.38 $M_\odot$ of ^{56}Ni. Of the two, the DDet model provides an excellent match to the data, while the DDT model light curve is broader than that of the observation.

Given the systematic uncertainties associated with the blackbody corrections used to derive the full bolometric luminosity, we performed an alternative comparison using pseudobolometric light curves. These were constructed by integrating the flux over the observed wavelength range (covering the u, g, and r bands) for both the observed SEDs and the model spectra. In this pseudobolometric analysis, we identify `ddt_2013_n1600` and `doubledet_2010_2` as the best-matching models (Figure 18. This result differs from the best matches obtained via the full bolometric light-curve comparison, underscoring the impact of blackbody correction on model selection. Notably, the `ddt_2013_n1600` model provides the best fit to the earliest epoch spectrum. However, although the integrated pseudobolometric luminosity shows good agreement, discrepancies remain in the individual bands. When aligned to the peak time of the r band, the synthetic u, g, and r light curves of these models do not simultaneously reproduce the detailed evolution observed in SN 2024aedt.

As shown in Figure 5, early light-curve behavior indicates a smooth power-law rise without an early excess (EEx) feature (although we acknowledge that an inconspicuous EEx occurring in the gap between the last nondetection and the first detection cannot be excluded). In the DDet models, the detonation of, e.g., a 0.055 $M_\odot$ He shell can produce clear EEx emissions in the light curves (U. M. Noebauer et al. 2017; K. Maeda et al. 2018). The absence of EEx in SN 2024aedt may suggest that the He shell mass is significantly lower or that the SN was viewing away from the detonation direction where the most inconspicuous EEx is expected, which has been proposed for interpreting normal SNe Ia without EEx features (K. J. Shen et al. 2021; W. Wu et al. 2025). The result is also supported by the relatively normal peak color and the lack of line blanking caused by IGE in the spectra. Alternatively, tension in early photometric evolution could be mitigated by an IME-dominated shell, which produces a peak color bluer than that of an IGE-dominated shell (M. R. Magee et al. 2021). Furthermore, C. Collins (2021) found that their synthetic photometry from the `ARTIS-NLTE` model can well reproduce the observations of SN 2011fe without the reddening seen in classic models. For the DDT model, a smooth rise is easy to reproduce (U. M. Noebauer et al. 2017), and it has also been used to explain other transitional events (e.g., C. Ashall et al. 2018).

For the spectral comparison, we quantify the similarity between observed spectra and the theoretical models by calculating the mean squared error (MSE) after normalization. The comparison was performed at similar epochs, using the peak of the bolometric light curve as the reference time for the model spectra. For each of our five observed spectra, we consider all model spectra within a ±2-day window of the observation epochs and identify the model with the lowest MSE as the best match. The results are presented in Figure 19.

The comparison shows that the premaximum spectrum of SN 2024aedt is well matched by the models in terms of line velocities, absorption strengths, and the overall continuum shape. The subsequent two spectra also show a relatively good match, though with larger deviations appearing at the red end compared to the blue end. The quality of the match for the final, latest-phase spectrum is poorer than for the earlier epochs. Statistically,

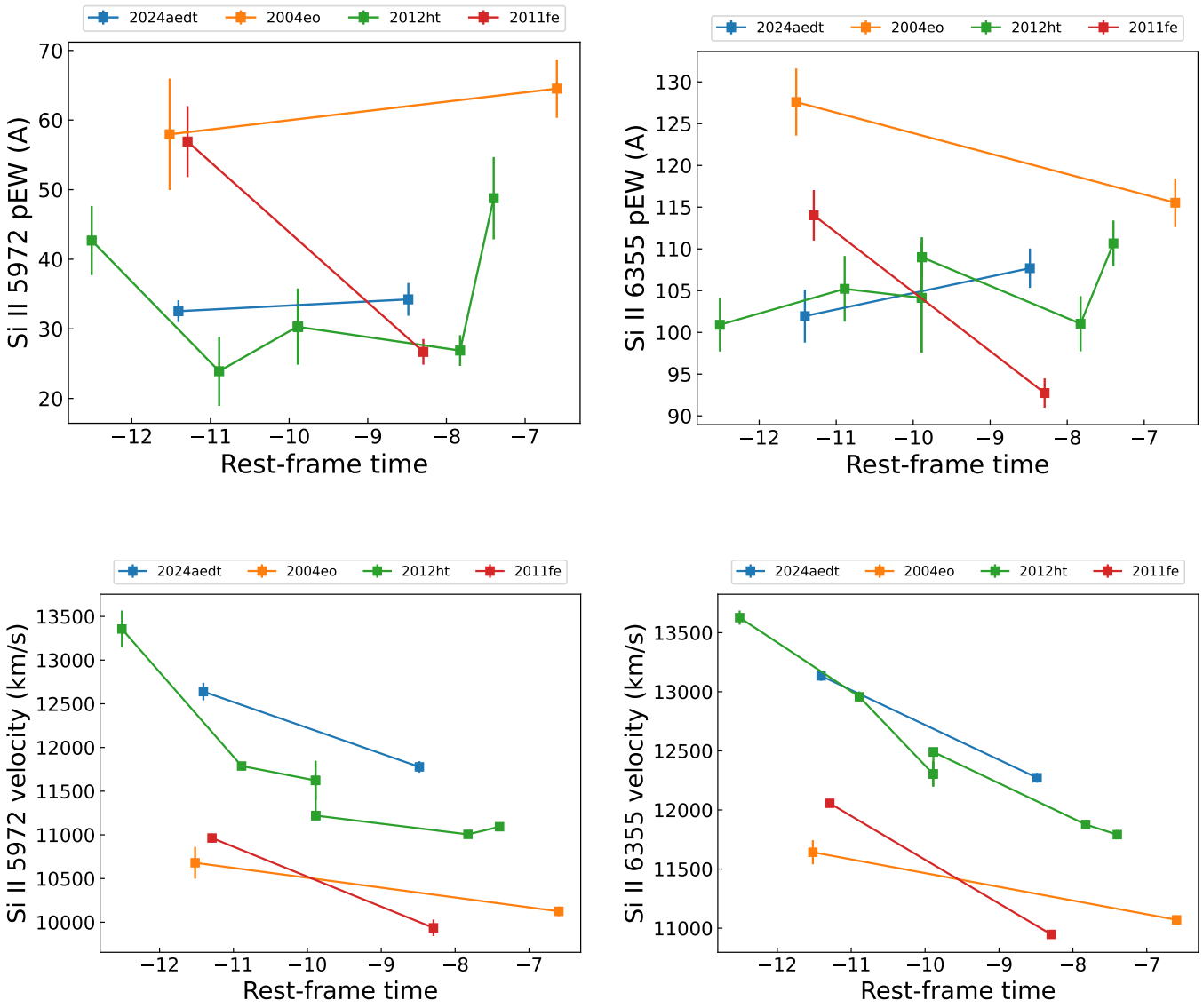

Figure 14. Evolution of the properties of the Si II doublet for SN 2024aedt and the comparison sample. The top panels show the pEW evolution for the Si II λ5972 (left) and Si II λ6355 (right) lines. The bottom panels show the corresponding velocity evolution measured from each line.

Table 1
Photometry of the Host Galaxy UGC 1325 in the Adopted Filter Set

Filter	AB Magnitude
GALEX NUV	16.737 ± 0.031
SDSS *u*	15.707 ± 0.040
SDSS *g*	13.510 ± 0.010
SDSS *r*	12.627 ± 0.006
SDSS *i*	12.132 ± 0.004
SDSS *z*	11.963 ± 0.005
2MASS *J*	10.704 ± 0.002
2MASS *H*	9.998 ± 0.003
2MASS K_s	9.734 ± 0.003
WISE W1	9.577 ± 0.013
WISE W2	9.593 ± 0.018
WISE W3	9.530 ± 0.056

Note. The measurements were obtained with the `hostphot` package.

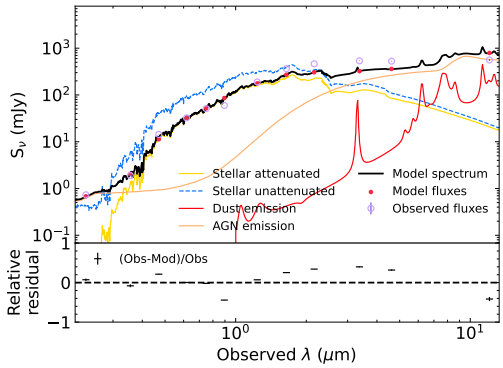

Figure 15. The best-fit SED model for the host galaxy UGC 1325, generated with `CIGALE`.

the DDT models provide a better overall fit to our spectral series. In four of the five epochs, the single best-matching model is a DDT model from I. R. Seitenzahl et al. (2013) and S. A. Sim et al. (2013). Furthermore, the majority of the top five best-fitting models in each epoch are also from the DDT scenario. A DDet model from M. Kromer et al. (2010) provides the best fit in only one epoch. We also considered the 1D DDet model from F. P. Callan et al. (2025), available in HESMA,

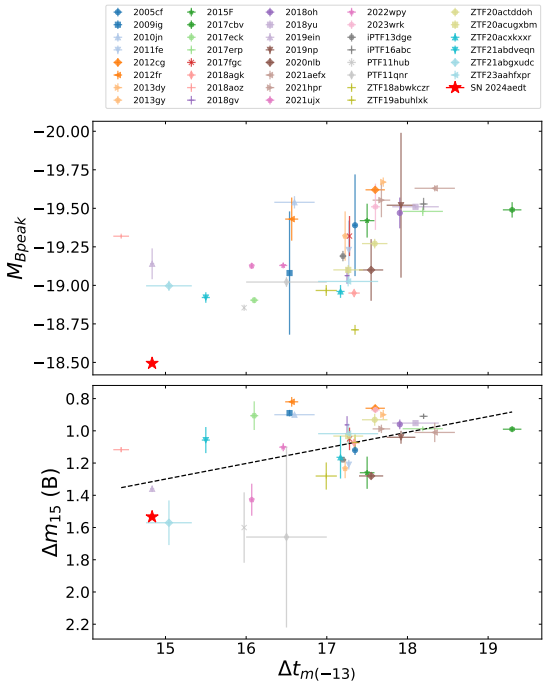

Figure 16. Top panel: $M_{B,\max}$ vs. $\Delta t_{m(-13)}$. Bottom panel: $\Delta m_{15}(B)$ vs. $\Delta t_{m(-13)}$. The position of SN 2024aedt is shown for comparison with the sample from W. Wu et al. (2025).

Table 2
Host Galaxy Morphological Type of Collected Transitional Sample.

SN	Host Type	Source
SN 2011iv	E1	C. Weidner et al. (2013)
SN 2007on	E1	(C. Weidner et al. 2013)
SN 2012ht	SBm	(H. B. Ann et al. 2015)
SN 2021rhu	S	(R. J. Buta 2019)
SN 2003hv	SA0^0(r)?	(G. de Vaucouleurs et al. 1991)
SN 2005am	SB(rs)a	(G. de Vaucouleurs et al. 1991)
SN 1998bp	E	(G. de Vaucouleurs et al. 1991)
SN 2015bp	SAB0^0?(rs)	(G. de Vaucouleurs et al. 1991)
SN 1986G	S0pec	(C. Weidner et al. 2013)
SN 2004eo	SB(s)ab	(G. de Vaucouleurs et al. 1991)
SN 2003gs	SB 0^+(rs)	(G. de Vaucouleurs et al. 1991)
iPTF13ebh	SAB0^-(r)?	(G. de Vaucouleurs et al. 1991)
SN 2009an	SB(s)a	(G. de Vaucouleurs et al. 1991)

Note. Data are from SIMBAD and NED.

which features a 0.04 $M_\odot$ He shell and 1.01 $M_\odot$ of ejecta. This model is constructed by radially averaging cells from the 3D model of S. Gronow et al. (2021; which had 0.018 $M_\odot$ of He and 0.83 $M_\odot$ of ejecta) within a solid-angle cone centered on the negative z-axis. While this model provides a good match to our second spectrum, it fails to reproduce the earliest one, showing significant blue-end suppression when normalized to redder wavelengths. This discrepancy is likely caused by the large amount of synthesized IGE in the model's outer layers, which is inconsistent with our observations, highlighting the crucial role of early-time spectra and blue-end photometry in constraining explosion scenarios. Consequently, a relatively thick He shell is disfavored for SN 2024aedt. This finding is consistent with the parameter space explored by A. Polin et al. (2019), where thin He shells ($<0.02\,M_\odot$) were shown to reproduce smooth early-time light curves, as well as appropriate color and spectroscopic

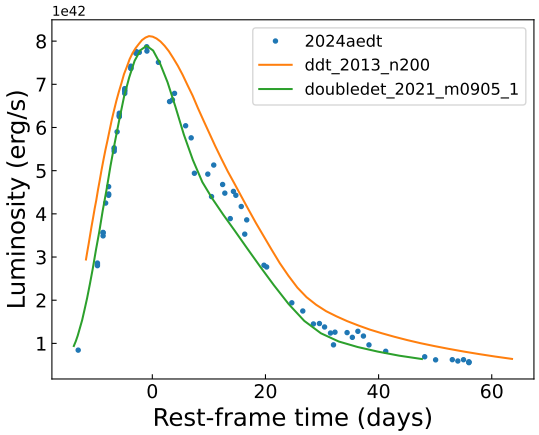

Figure 17. Best-fitting model light curves from HESMA for SN 2024aedt. The observed bolometric light curve (blue circles) is shown alongside the best-fitting DDT (orange) and DDet (green) models.

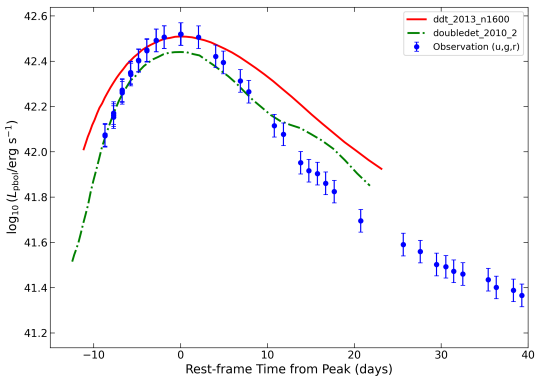

Figure 18. Comparison of the pseudobolometric light curve of SN 2024aedt (blue circles) with selected explosion models. The red solid line represents the best-fit DDT model, and the green dotted–dashed line represents the DDet model. The pseudobolometric luminosity is integrated over the wavelength range covered by the u, g, and r bands. For the observations, the light curve was derived by integrating the SED approximated from the u, g, and r photometry.

features. However, whether such low-mass shells can successfully initiate a detonation remains under debate (K. Iwata & K. Maeda 2024).

In addition, the apparent statistical preference for the DDT scenario must be interpreted with caution. The apparent good fit of the DDT scenario is undermined by two key problems. First, the best-fitting DDT model is not consistent across all epochs, with the required number of ignition kernels varying between epochs. This is also found in S. A. Sim et al. (2013). They note that the evolution of their synthetic spectra is too quick, an imperfection also demonstrated by their SNID matching results. We further match each of the best-matching DDT models against the entire observed time series, focusing mainly on the premaximum epochs. The match for the first epoch always yields relatively good results, but the subsequent epoch shows significant underestimates of the flux at the blue end (the ddt_2013_n1 model does not have a match with the first epoch, but it shows a good match with the second one). This corresponds to the redder color found in S. A. Sim et al. (2013) owing to excessive line blanketing caused by the stable IGEs formed in the deflagration process. The elements float to the surface and dominate the layers with intermediate velocities, suggesting that SN 2024aedt either experiences a

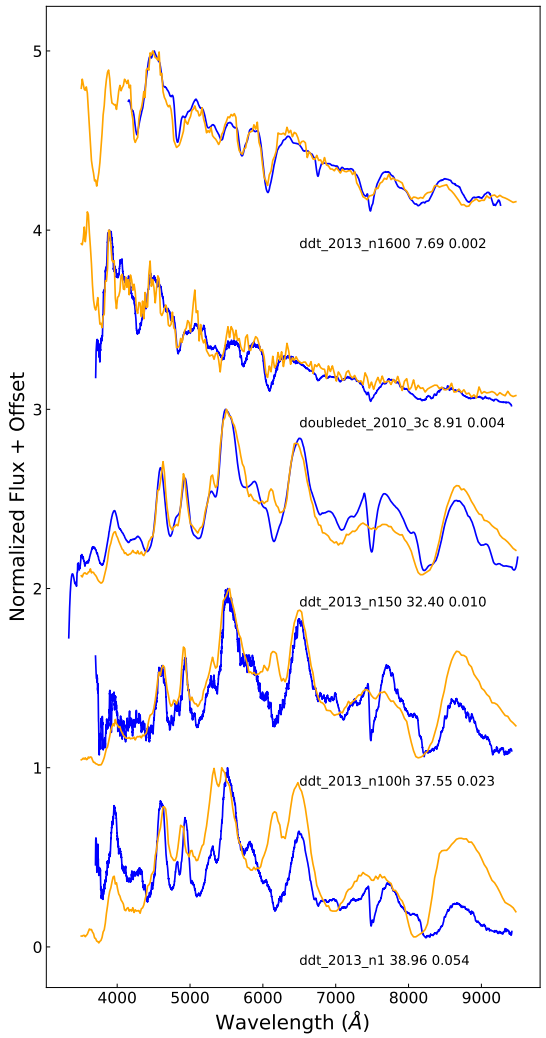

Figure 19. Best-match HESMA model spectra for each observed epoch of SN 2024aedt. The observed spectra are shown in blue, and the model spectra are shown in orange. The top two display the two premaximum phases, and the bottom three show the three post-maximum phases. The best-fit model name, phase, and MSE are indicated below each spectrum.

lesser extent of deflagration than the model predicts (which creates difficulties for the light-curve matching, since models with fewer ignition kernels exhibit higher luminosity) or is caused by other mechanisms without deflagration. Second, the models that provide the best fit to our crucial premaximum spectra are noted by S. A. Sim et al. (2013) to be a poor match for subluminous SNe based on their photometric properties. For the DDet scenario, the inherent asymmetry of explosions means that significant viewing angle effects are expected, and their angle-averaged model spectra are not representative of a single observational line of sight. However, there are no angle-dependent synthetic observations available for the selected scenarios in HESMA.

Far from being a simple caveat, the asymmetry of the DDet scenario provides a natural explanation for the observed diversity in early-time spectral features (such as the blue-end variations in the early-time spectra) across the transitional population. The DDet can potentially unify the transitional class within a single physical framework and possibly include the normal and SN 1991bg–like populations as well through different distributions of its underlying physical parameters. On the other hand, the viewing angle effects for most DDT models are less significant (with the exception of models with few ignition kernels, e.g., the N3 model in S. A. Sim et al. 2013). Given these considerations, the DDet model with a thin He shell can offer a compelling and unified explanation for the entire transitional group. The diversity found in the early-time line velocities and blue-end absorption features (Figures 10 and 12) contrasts with the greater homogeneity observed in the post-maximum spectra, illustrating the importance and diagnostic power of early-phase observations for constraining progenitor properties and explosion mechanisms. Detailed analysis of early-time observations of a larger sample is required to test this hypothesis.

5. Conclusion

In this paper, we present a comprehensive analysis of the transitional SN Ia SN 2024aedt. The photometric evolution shows a clear power-law rise consistent with an expanding fireball model. The peak absolute magnitude $M_B = -18.49 \pm 0.03$ mag, decline rate $\Delta m_{15}(B) = 1.53 \pm 0.36$ mag, and early color evolution place it in the parameter space between normal and SN 1991bg–like SN Ia populations, along with other transitional events. From the modeling of light curves, we derive a synthesized ^{56}Ni mass of $0.414 \pm 0.042\,M_{\odot}$. Spectroscopically, measurements of the pEW and velocity of the Si II lines in the early spectra show that the pEW evolution of transitional SNe, including SN 2024aedt, is much slower and flatter than that of normal SNe Ia at similar phases, consistent with their evolution in the Branch diagram CL region. For the spectral evolution, SN 2024aedt shows an overall similarity to other transitional objects. However, a detailed comparison reveals diversity in the early-time blue features, which becomes more homogeneous at later phases. Based on our comparison with available models, we find that both the DDT and DDet scenarios are capable of reproducing the observed properties of SN 2024aedt to a reasonable extent. Further detailed analysis and a larger sample of observations with improved early-phase coverage are required to distinguish between these models.

With the continuing WFST survey operation, a larger population of transitional SNe, similar to SN 2024aedt, is expected to be discovered. The survey's high-cadence strategy and depth enable the early discovery of valuable transients and prompt follow-up observations. With this greatly enriched sample, it will be possible to precisely constrain the parameter space that connects the normal and subluminous populations. Moreover, statistical studies of early light curves and color curves may reveal diversity within the transitional class, providing crucial constraints on the progenitor channels and explosion mechanisms of SNe Ia.

Acknowledgments

This work was supported by the National Key R&D Program of China (grant No. 2023YFA1608100), the National Natural Science Foundation of China (grant No. 12393811, 12233008), and the Strategic Priority Research Program of the Chinese Academy of Science (grant No. XDB0550300). J.J. acknowledges support from the Japan Society for the Promotion of Science (JSPS) KAKENHI grants JP22K14069. K.M. acknowledges support from JSPS KAKENHI grants JP24KK0070 and 24H01810.

K.M. and H.K. acknowledge support from the JSPS bilateral JPJSBP120229923. L.G. acknowledges financial support from AGAUR, CSIC, MCIN, and AEI 10.13039/501100011033 under projects PID2023-151307NB-I00, PIE 20215AT016, CEX2020-001058-M, ILINK23001, COOPB2304, and 2021-SGR-01270.

Based on observations made with the Nordic Optical Telescope, owned in collaboration by the University of Turku and Aarhus University and operated jointly by Aarhus University, the University of Turku, and the University of Oslo, representing Denmark, Finland, and Norway; the University of Iceland; and Stockholm University at the Observatorio del Roque de los Muchachos, La Palma, Spain, of the Instituto de Astrofisica de Canarias. The NOT data were obtained under program ID P70-018. This work has made use of data from the Asteroid Terrestrial-impact Last Alert System (ATLAS) project. The ATLAS project is primarily funded to search for near-Earth asteroids through NASA grants NN12AR55G, 80NSSC18K0284, and 80NSSC18K1575; by-products of the NEO search include images and catalogs from the survey area. This work was partially funded by Kepler/K2 grant J1944/80NSSC19K0112, HST GO-15889, and STFC grants ST/T000198/1 and ST/S006109/1. The ATLAS science products have been made possible through the contributions of the University of Hawaii Institute for Astronomy, the Queen's University Belfast, the Space Telescope Science Institute, the South African Astronomical Observatory, and the Millennium Institute of Astrophysics (MAS), Chile.

This research made use of Photutils, an Astropy package for detection and photometry of astronomical sources (L. Bradley et al. 2024).

The Pan-STARRS1 Surveys (PS1) and the PS1 public science archive have been made possible through contributions by the Institute for Astronomy, the University of Hawaii, the Pan-STARRS Project Office, the Max-Planck Society and its participating institutes, the Max Planck Institute for Astronomy, Heidelberg and the Max Planck Institute for Extraterrestrial Physics, Garching, Johns Hopkins University, Durham University, the University of Edinburgh, the Queen's University Belfast, the Harvard-Smithsonian Center for Astrophysics, the Las Cumbres Observatory Global Telescope Network Incorporated, the National Central University of Taiwan, the Space Telescope Science Institute, the National Aeronautics and Space Administration under grant No. NNX08AR22G issued through the Planetary Science Division of the NASA Science Mission Directorate, the National Science Foundation grant No. AST-1238877, the University of Maryland, Eotvos Lorand University (ELTE), the Los Alamos National Laboratory, and the Gordon and Betty Moore Foundation.

This work makes use of observations from the Las Cumbres Observatory global telescope network.

Based on observations obtained with the Apache Point Observatory 3.5 m telescope, which is owned and operated by the Astrophysical Research Consortium.

This paper includes data gathered with the 6.5 meter Magellan Telescopes located at Las Campanas Observatory, Chile.

This work made use of the Heidelberg Supernova Model Archive (HESMA), https://hesma.h-its.org.

Facilities: WFST:2.5m, ARC, NOT, ATLAS, LCOGT, Magellan:Baade.

Software: Astropy (Astropy Collaboration et al. 2013, 2018; Astropy Collaboration et al. 2022), Source Extractor (E. Bertin & S. Arnouts 1996), SWarp (E. Bertin et al. 2002), astroquery (A. Ginsburg et al. 2019), Photutils (L. Bradley et al. 2024), PyKOSMOS (J. Davenport 2021), superbol (M. Nicholl 2018), SALT2 (J. Guy et al. 2007), MOSFiT (J. Guillochon et al. 2018), CIGALE (M. Boquien et al. 2019), SNooPy (C. R. Burns et al. 2011).

Appendix A
Fringe Correction Procedure

The LCO images, particularly in the z band and to a lesser extent in the i band, were affected by significant fringing patterns. To correct for this, a fringe correction template was constructed. The method assumes a linear relationship for the fringe pattern intensity at any given pixel across different images. We used archival images from the `LCO Science Archive` that matched the observatory, telescope, instrument, and filter of our science images but targeted different sky locations. Frames containing bright or extended sources near the center were excluded.

The correction process involved the following steps. First, each image was normalized by its exposure time, divided into a grid of 20 × 20 pixel blocks, and the mean value of each block was calculated. A single image was then chosen as a reference frame. For every other image, a scatter plot was generated by plotting the mean block values of the reference frame on the x-axis against the corresponding values from the other image on the y-axis. These plots typically exhibit a multibranched structure: divergent branches correspond to blocks containing astronomical sources, while a tight, linear branch near the origin represents blocks containing only background flux. This linear branch reflects the true scaling relationship of the fringe pattern between the two images. A linear regression was performed exclusively on this branch to determine the scaling factor and offset needed to match the backgrounds.

After all template images were scaled to the reference frame, they were median-combined to create a master fringe template. This process removes most astronomical sources. Our science target was deliberately positioned at an offset from the image center, ensuring that our photometry was unaffected by potential residual artifacts at the center of the template. While this method proved effective for most of the data, a subset of images could not be corrected satisfactorily. These included frames with significant residual patterns post-subtraction or those from which a reliable fringe pattern could not be extracted. To ensure the quality of the final light curve, these problematic images were excluded from the analysis.

Appendix B
Corner Plot of MOSFiT

In Appendix B, we present the parameter constraints from our `MOSFIT` modeling. Figure B1 shows the corner plot representing the posterior probability distributions and the correlations between the physical parameters derived for SN 2024aedt.

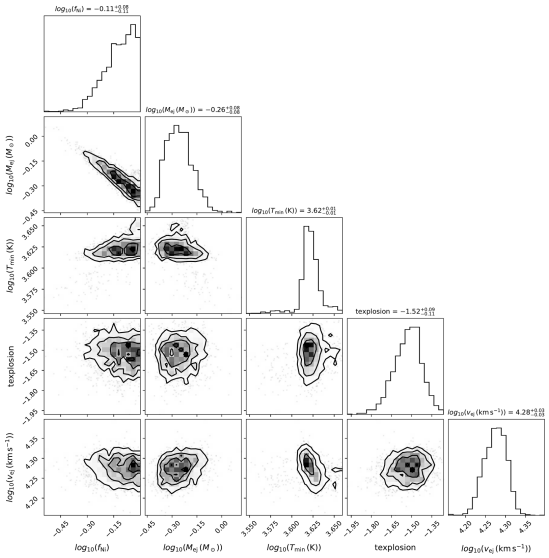

Figure B1. Corner plot showing the posterior probability distributions for the parameters of the MOSFiT fit.

Appendix C
Photometry of SN 2024aedt

In Appendix C, we provide supplementary analysis and data for SN 2024aedt. Specifically, the complete photometric data are summarized in Table 3.

Table 3
Detections and 5σ Upper Limits of SN 2024aedt, Corrected for MW Extinction

Source	Type	MJD	Filter	Apparent Magnitude	Phase
WFST	DET	60659.526	g	18.961 ± 0.022	−12.946
WFST	DET	60659.559	g	18.871 ± 0.025	−12.914
WFST	DET	60660.525	g	18.348 ± 0.013	−11.965
WFST	DET	60661.516	g	17.894 ± 0.039	−10.992
WFST	DET	60662.526	g	17.547 ± 0.004	−10.001
WFST	DET	60662.559	g	17.515 ± 0.005	−9.969
WFST	DET	60663.531	u	18.042 ± 0.021	−9.013
WFST	DET	60663.579	g	17.187 ± 0.003	−8.967
WFST	DET	60663.655	r	17.191 ± 0.005	−8.892
WFST	DET	60663.655	r	17.215 ± 0.005	−8.891

(This table is available in its entirety in machine-readable form in the online article.)

ORCID iDs

Ji-an Jiang https://orcid.org/0000-0002-9092-0593
Xu Kong https://orcid.org/0000-0002-7660-2273
Keiichi Maeda https://orcid.org/0000-0003-2611-7269
Hanindyo Kuncarayakti https://orcid.org/0000-0002-1132-1366
Lluís Galbany https://orcid.org/0000-0002-1296-6887
Saurabh W. Jha https://orcid.org/0000-0001-8738-6011
Peter Yoachim https://orcid.org/0000-0003-2874-6464
Weiyu Wu https://orcid.org/0009-0003-9474-8457
Zhengyan Liu https://orcid.org/0000-0002-2242-1514
Andrew J. Connolly https://orcid.org/0000-0001-5576-8189
Lei Hu https://orcid.org/0000-0001-7201-1938
Weiyu Ding https://orcid.org/0000-0003-0230-4596
Lulu Fan https://orcid.org/0000-0003-4200-4432
Yongquan Xue https://orcid.org/0000-0002-1935-8104
Wen Zhao https://orcid.org/0000-0002-1330-2329
Xianzhong Zheng https://orcid.org/0000-0003-3728-9912
Qingfeng Zhu https://orcid.org/0000-0003-0694-8946

References

Abdurro'uf, Accetta, K., Aerts, C., et al. 2022, ApJS, 259, 35
Aghanim, N., Akrami, Y., Ashdown, M., et al. 2020, A&A, 641, A6
Andrew Howell, D., Sullivan, M., Nugent, P. E., et al. 2006, Natur, 443, 308
Ann, H. B., Seo, M., & Ha, D. K. 2015, ApJS, 217, 27
Ashall, C., Mazzali, P. A., Stritzinger, M. D., et al. 2018, MNRAS, 477, 153
Astropy Collaboration, Price-Whelan, A. M., Lim, P. L., et al. 2022, ApJ, 935, 167
Astropy Collaboration, Price-Whelan, A. M., Sipőcz, B. M., et al. 2018, AJ, 156, 123
Astropy Collaboration, Robitaille, T. P., Tollerud, E. J., et al. 2013, A&A, 558, A33
Axelrod, T., Kantor, J., Lupton, R. H., & Pierfederici, F. 2010, SPIE, 7740, 774015
Bertin, E., & Arnouts, S. 1996, A&AS, 117, 393
Bertin, E., Mellier, Y., Radovich, M., et al. 2002, ASPC, 281, 228
Bildsten, L., Shen, K. J., Weinberg, N. N., & Nelemans, G. 2007, ApJL, 662, L95
Blondin, S., Matheson, T., Kirshner, R. P., et al. 2012, AJ, 143, 126
Boquien, M., Burgarella, D., Roehlly, Y., et al. 2019, A&A, 622, A103
Bosch, J., Armstrong, R., Bickerton, S., et al. 2018, PASJ, 70, S5
Bradley, L., Sipőcz, B., Robitaille, T., et al. 2024, astropy/photutils: 2.0.2, v2.0.2, Zenodo, doi:10.5281/zenodo.13989456
Branch, D., Dang, L. C., Hall, N., et al. 2006, PASP, 118, 560
Brown, T. M., Baliber, N., Bianco, F. B., et al. 2013, PASP, 125, 1031
Bruzual, G., & Charlot, S. 2003, MNRAS, 344, 1000
Burgaz, U., Maguire, K., Dimitriadis, G., et al. 2025, A&A, 694, A9
Burns, C. R., Parent, E., Phillips, M. M., et al. 2018, ApJ, 869, 56
Burns, C. R., Stritzinger, M., Phillips, M. M., et al. 2011, AJ, 141, 19
Burns, C. R., Stritzinger, M., Phillips, M. M., et al. 2014, ApJ, 789, 32
Buta, R. J. 2019, MNRAS, 488, 590
Cai, M., Xu, Z., Fan, L., et al. 2025, arXiv:2501.15018
Callan, F. P., Collins, C. E., Sim, S. A., et al. 2025, MNRAS, 539, 1404
Cartier, R., Sullivan, M., Firth, R. E., et al. 2017, MNRAS, 464, 4476
Chabrier, G. 2003, PASP, 115, 763
Chakradhari, N. K., Sahu, D. K., Srivastav, S., & Anupama, G. C. 2014, MNRAS, 443, 1663
Chambers, K. C., Magnier, E. A., Metcalfe, N., et al. 2016, arXiv:1612.05560
Charlot, S., & Fall, S. M. 2000, ApJ, 539, 718
Collins, C. 2021, PhD thesis , Queen's University Belfast
Contreras, C., Hamuy, M., Phillips, M. M., et al. 2010, AJ, 139, 519
Davenport, J. 2021, PyKOSMOS: A Python-Based Spectral Reduction Suite for KOSMOS at APO, Zenodo, doi:10.5281/zenodo.5120786
de Vaucouleurs, G., de Vaucouleurs, A., Corwin, H. G., Jr., et al. 1991, Third Reference Catalogue of Bright Galaxies (Springer)
Deckers, M., Maguire, K., Shingles, L., et al. 2025, A&A, 694, A12
Desai, D. D., Kochanek, C. S., Shappee, B. J., et al. 2024, MNRAS, 530, 5016
Dhawan, S., Leibundgut, B., Spyromilio, J., & Blondin, S. 2016, A&A, 588, A84
Dimitriadis, G., Burgaz, U., Deckers, M., et al. 2025, A&A, 694, A10
Djupvik, A. A., & Andersen, J. 2010, in Astrophysics and Space Science Proc., Highlights of Spanish Astrophysics V, Vol. 14, ed. J. M. Diego et al., 211, doi:10.1007/978-3-642-11250-8_21
Draine, B. T., Aniano, G., Krause, O., et al. 2014, ApJ, 780, 172
Filippenko, A. V., Richmond, M. W., Branch, D., et al. 1992a, AJ, 104, 1543
Filippenko, A. V., Richmond, M. W., Matheson, T., et al. 1992b, ApJL, 384, L15
Firth, R. E., Sullivan, M., Gal-Yam, A., et al. 2015, MNRAS, 446, 3895
Fitzpatrick, E. L. 1999, PASP, 111, 63
Fitzpatrick, E. L., & Massa, D. 2007, ApJ, 663, 320
Flewelling, H. A., Magnier, E. A., Chambers, K. C., et al. 2020, ApJS, 251, 7
Folatelli, G., Morrell, N., Phillips, M. M., et al. 2013, ApJ, 773, 53
Gall, C., Stritzinger, M. D., Ashall, C., et al. 2018, A&A, 611, A58
Ganeshalingam, M., Li, W., & Filippenko, A. V. 2013, MNRAS, 433, 2240
Ganeshalingam, M., Li, W., Filippenko, A. V., et al. 2012, ApJ, 751, 142

Garavini, G., Folatelli, G., Goobar, A., et al. 2004, AJ, 128, 387
Ginsburg, A., Sipőcz, B. M., Brasseur, C. E., et al. 2019, AJ, 157, 98
González-Gaitán, S., Perrett, K., Sullivan, M., et al. 2011, ApJ, 727, 107
Graham, M. L., Kumar, S., Hosseinzadeh, G., et al. 2017, MNRAS, 472, 3437
Gronow, S., Collins, C. E., Sim, S. A., & Röpke, F. K. 2021, A&A, 649, A155
Guillochon, J., Nicholl, M., Villar, V. A., et al. 2018, ApJS, 236, 6
Guillochon, J., Parrent, J., Kelley, L. Z., & Margutti, R. 2017, ApJ, 835, 64
Guy, J., Astier, P., Baumont, S., et al. 2007, A&A, 466, 11
Hamuy, M., Phillips, M. M., Suntzeff, N. B., et al. 2003, Natur, 424, 651
Harvey, L., Maguire, K., Magee, M. R., et al. 2023, MNRAS, 522, 4444
Hicken, M., Challis, P., Jha, S., et al. 2009, ApJ, 700, 331
Hoeflich, P., Hsiao, E. Y., Ashall, C., et al. 2017, ApJ, 846, 58
Hsiao, E. Y., Burns, C. R., Contreras, C., et al. 2015, A&A, 578, A9
Hu, M., Hu, L., Jiang, J.-a., et al. 2022, Univ, 9, 7
Iben, I., Jr., & Tutukov, A. V. 1984, ApJS, 54, 335
Ivezić, Ž., Kahn, S. M., Tyson, J. A., et al. 2019, ApJ, 873, 111
Iwata, K., & Maeda, K. 2024, PhRvL, 133, 121201
Jha, S. 2002, PhD thesis, Harvard University, Massachusetts
Jha, S., Branch, D., Chornock, R., et al. 2006a, AJ, 132, 189
Jha, S., Kirshner, R. P., Challis, P., et al. 2006b, AJ, 131, 527
Jiang, J.-a., Doi, M., Maeda, K., et al. 2017, Natur, 550, 80
Jiang, J.-a., Doi, M., Maeda, K., & Shigeyama, T. 2018, ApJ, 865, 149
Jiang, J.-a., Maeda, K., Kawabata, M., et al. 2021, ApJL, 923, L8
Kasen, D. 2006, ApJ, 649, 939
Kasen, D., Röpke, F. K., & Woosley, S. E. 2009, Natur, 460, 869
Kawabata, M., Maeda, K., Yamanaka, M., et al. 2020, ApJ, 893, 143
Khokhlov, A. M. 1991, A&A, 245, 114
Krisciunas, K., Hastings, N. C., Loomis, K., et al. 2000, ApJ, 539, 658
Krisciunas, K., Marion, G. H., Suntzeff, N. B., et al. 2009, AJ, 138, 1584
Kromer, M., Ohlmann, S. T., & Roepke, F. K. 2017, MmSAI, 88, 312
Kromer, M., Sim, S. A., Fink, M., et al. 2010, ApJ, 719, 1067
Leloudas, G., Stritzinger, M. D., Sollerman, J., et al. 2009, A&A, 505, 265
Maeda, K., Jiang, J.-a., Shigeyama, T., & Doi, M. 2018, ApJ, 861, 78
Magee, M. R., Maguire, K., Kotak, R., & Sim, S. A. 2021, MNRAS, 502, 3533
Martin, D. C., Fanson, J., Schiminovich, D., et al. 2005, ApJ, 619, L1
Masci, F. J., Laher, R. R., Rusholme, B., et al. 2023, arXiv:2305.16279
Matheson, T., Kirshner, R. P., Challis, P., et al. 2008, AJ, 135, 1598
Miller, A. A., Yao, Y., Bulla, M., et al. 2020, ApJ, 902, 47
Morrell, N., Burn, C., Xiao, H., & Hoogendam, W. 2024, TNSCR, 2024-4946, 1
Müller-Bravo, T. E., & Galbany, L. 2022, JOSS, 7, 4508
Nadyozhin, D. K. 1994, ApJS, 92, 527
Nicholl, M. 2018, RNAAS, 2, 230
Noebauer, U. M., Kromer, M., Taubenberger, S., et al. 2017, MNRAS, 472, 2787
Nomoto, K. 1982, ApJ, 253, 798
Ogawa, M., Maeda, K., & Kawabata, M. 2023, ApJ, 955, 49
Olling, R. P., Mushotzky, R., Shaya, E. J., et al. 2015, Natur, 521, 332
Pastorello, A., Mazzali, P. A., Pignata, G., et al. 2007, MNRAS, 377, 1531
Pereira, R., Thomas, R. C., Aldering, G., et al. 2013, A&A, 554, A27
Perlmutter, S., Aldering, G., Goldhaber, G., et al. 1999, ApJ, 517, 565
Perlmutter, S., Gabi, S., Goldhaber, G., et al. 1997, ApJ, 483, 565
Phillips, M. M. 1993, ApJ, 413, L105
Phillips, M. M., Lira, P., Suntzeff, N. B., et al. 1999, AJ, 118, 1766
Phillips, M. M., Phillips, A. C., Heathcote, S. R., et al. 1987, PASP, 99, 592
Polin, A., Nugent, P., & Kasen, D. 2019, ApJ, 873, 84
Riess, A. G., Filippenko, A. V., Challis, P., et al. 1998, AJ, 116, 1009
Riess, A. G., Filippenko, A. V., Li, W., et al. 1999, AJ, 118, 2675
Rigault, M., Smith, M., Goobar, A., et al. 2025, A&A, 694, A1
Sahu, D. K., Anupama, G. C., & Anto, P. 2013, MNRAS, 430, 869
Savitzky, A., & Golay, M. J. E. 1964, AnaCh, 36, 1627
Schlafly, E. F., & Finkbeiner, D. P. 2011, ApJ, 737, 103
Seitenzahl, I. R., Ciaraldi-Schoolmann, F., Röpke, F. K., et al. 2013, MNRAS, 429, 1156
Senzel, R., Maguire, K., Burgaz, U., et al. 2025, A&A, 694, A14
Shen, K. J., Boos, S. J., Townsley, D. M., & Kasen, D. 2021, ApJ, 922, 68
Shingles, L., Smith, K. W., Young, D. R., et al. 2021, TNSAN, 7, 1
Silverman, J. M., Kong, J. J., & Filippenko, A. V. 2012, MNRAS, 425, 1819
Silverman, J. M., Nugent, P. E., Gal-Yam, A., et al. 2013, ApJS, 207, 3
Sim, S. A., Seitenzahl, I. R., Kromer, M., et al. 2013, MNRAS, 436, 333
Skrutskie, M. F., Cutri, R. M., Stiening, R., et al. 2006, AJ, 131, 1163
Smith, K. W., Smartt, S. J., Young, D. R., et al. 2020, PASP, 132, 085002
Stalevski, M., Fritz, J., Baes, M., Nakos, T., & Popović, L. Č. 2012, MNRAS, 420, 2756
Stalevski, M., Ricci, C., Ueda, Y., et al. 2016, MNRAS, 458, 2288
Taubenberger, S. 2017, The Extremes of Thermonuclear Supernovae (Springer), 317
Taubenberger, S., Hachinger, S., Pignata, G., et al. 2008, MNRAS, 385, 75
Theureau, G., Hanski, M. O., Coudreau, N., Hallet, N., & Martin, J.-M. 2007, A&A, 465, 71
Tonry, J. L., Denneau, L., Heinze, A. N., et al. 2018, PASP, 130, 064505
Tonry, J., Denneau, L., Weiland, H., et al. 2024, TNSTR, 2024-4922, 1
Tutukov, A. V., & Yungelson, L. R. 1981, NInfo, 49, 3
Uddin, S. A., Burns, C. R., Phillips, M. M., et al. 2024, ApJ, 970, 72
Vincenzi, M., Brout, D., Armstrong, P., et al. 2024, ApJ, 975, 86
Wang, T., Liu, G., Cai, Z., et al. 2023, SCPMA, 66, 109512
Webbink, R. F. 1984, ApJ, 277, 355
Wegner, G., Bernardi, M., Willmer, C. N. A., et al. 2003, AJ, 126, 2268
Weidner, C., Ferreras, I., Vazdekis, A., & La Barbera, F. 2013, MNRAS, 435, 2274
Whelan, J., & Iben, I., Jr. 1973, ApJ, 186, 1007
Wood-Vasey, W. M., Friedman, A. S., Bloom, J. S., et al. 2008, ApJ, 689, 377
Wright, E. L., Eisenhardt, P. R. M., Mainzer, A. K., et al. 2010, AJ, 140, 1868
Wu, W., Jiang, J.-a., Meng, D., et al. 2025, ApJ, 991, 148
Wyatt, S. D., Sand, D. J., Hsiao, E. Y., et al. 2021, ApJ, 914, 57
Xi, G., Wang, X., Li, W., et al. 2022, MNRAS, 517, 4098
Yaron, O., & Gal-Yam, A. 2012, PASP, 124, 668
Zhao, X., Maeda, K., Wang, X., & Sai, H. 2020, MNRAS, 503, 4667